



**HAL**  
open science

## The microstructure of layered ultramafic cumulates: Case study of the Bear Creek intrusion, Trinity ophiolite, California, USA

Hadrien Henry, Mary-Alix Kaczmarek, Georges Ceuleneer, Romain Tilhac,  
William L. Griffin, Suzanne Y. O'Reilly, Michel Grégoire, Elisabeth Le Sueur

### ► To cite this version:

Hadrien Henry, Mary-Alix Kaczmarek, Georges Ceuleneer, Romain Tilhac, William L. Griffin, et al..  
The microstructure of layered ultramafic cumulates: Case study of the Bear Creek intrusion, Trinity  
ophiolite, California, USA. *Lithos*, 2021, 388, 10.1016/j.lithos.2021.106047 . insu-03661466

**HAL Id: insu-03661466**

**<https://insu.hal.science/insu-03661466>**

Submitted on 10 Mar 2023

**HAL** is a multi-disciplinary open access archive for the deposit and dissemination of scientific research documents, whether they are published or not. The documents may come from teaching and research institutions in France or abroad, or from public or private research centers.

L'archive ouverte pluridisciplinaire **HAL**, est destinée au dépôt et à la diffusion de documents scientifiques de niveau recherche, publiés ou non, émanant des établissements d'enseignement et de recherche français ou étrangers, des laboratoires publics ou privés.



Distributed under a Creative Commons Attribution - NonCommercial 4.0 International License



## 22 **Abstract**

23 In the Trinity ophiolite, California, USA, several mafic-ultramafic plutons intruded a  
24 peridotitic host 435 to 405 m.y. ago in a tectonic setting interpreted as an arc-related  
25 spreading centre. One of these intrusions, in the Bear Creek area, exposes basal ultramafic  
26 cumulates with igneous layering comprising an alternation of uncommonly thin (down to a  
27 few mm) layers of dunite, peridotite and pyroxenite that might be specific to this tectonic  
28 setting. These layers offer an excellent opportunity to characterise the microstructure of  
29 uncommon cumulates from the lower crust using EBSD (Electron Backscatter Diffraction).  
30 This “high-frequency” layering rests on underlying lherzolites and grades upward to more  
31 massive pyroxenites (i.e. clinopyroxenites with minor olivine-rich layers). Our field  
32 observations and data from the Bear Creek cumulates together with the preservation of  
33 magmatic features suggest the environment was tectonically stable after the emplacement of  
34 the cumulates. A detailed microstructural investigation of all minerals from the Bear Creek  
35 cumulates allows us to decipher their magmatic and plastic deformation history. In a  
36 structural reference frame defined by the compositional layering and the elongation direction  
37 of the surrounding host peridotites, olivine in the cumulates presents a [010]-fibre fabric and  
38 rarely a [001](010) fabric. Clinopyroxene shows a concentration of [010] axes normal to the  
39 layering plane with [100] and [001] defining girdles. Orthopyroxene mostly has a fabric with  
40 [100] and/or [010] subnormal to the layering plane and [001] scattered along a girdle in the  
41 plane of layering. All minerals show a strong fabric. We interpret the formation of the  
42 developed planar microstructures as a result of magmatic processes, with high contribution of  
43 crystal settling. To a lesser extent, compaction could have been operating and may be linked  
44 to the rare evidence of plastic deformation. Clusters of axes within the girdles of olivine and  
45 pyroxene CPOs preferentially appear close to the direction of elongation of the surrounding  
46 peridotites (i.e. N115°). EBSD analysis of the shape-preferred orientation of Bear Creek’s

47 minerals revealed a preferential alignment of the olivine and cpx long axis with the N°115  
48 direction. This magmatic lineation and the preferred direction in the CPOs girdles are both  
49 consistent with the stretching lineation acquired during solid-state deformation by the mantle  
50 peridotite of the Trinity ophiolite. We suggest that a weak magma flux early on and/or an  
51 ongoing but limited regional stress could be responsible for these clusters. Although a direct  
52 coupling between asthenospheric flow and magmatic flow cannot be invoked in this context  
53 of melt intrusion in the lithosphere, this result highlights that the stress field applied on the  
54 mantle could have been still active and similar during the formation of Bear Creek intrusion.  
55 Our new field and microstructural data, together with previously presented petrological data,  
56 fit a scenario for the evolution of the Trinity ophiolite in which a mantle segment was  
57 intruded by a single large batch of primitive boninitic-andesitic melt. Our results emphasise  
58 the importance of considering the initial magmatic microstructures and the original shape  
59 anisotropy when investigating later deformation in ultramafic rocks.

60

61

62 **Key words:**

63 **Magmatic fabric; Cumulate suite ; Trinity Ophiolite ; Plastic deformation ; Peridotite**  
64 **and pyroxenite EBSD ; Compaction of cumulates**

65

66 **1. Introduction**

67

68 In the past decades, pyroxenites have been the subject of numerous studies as their  
69 geochemical composition and microstructure provide important clues to petrological  
70 processes related to the development of heterogeneities in the Earth's upper mantle (e.g.  
71 Bodinier and Godard, 2003; O'Reilly and Griffin, 2013). Mineral fabrics in upper-mantle  
72 peridotites and pyroxenites are commonly interpreted as clues to solid-state ductile  
73 deformation that occurred by mechanisms such as dislocation and diffusion creep (e.g. Avé  
74 Lallemand and Carter, 1970; Frets et al., 2012; Nicolas and Christensen, 1987). When formed  
75 by dislocation creep, mineral fabrics will reflect the dominant slip system (or a combination  
76 of multiple slip systems each having a specific activity) that was active during the  
77 deformation episode (e.g. Ismaïl and Mainprice, 1998; Karato, 2008). The dependence of the  
78 activation of a slip system on parameters such as temperature, pressure, chemical  
79 composition or the presence of water in the mineral structure, which has been demonstrated  
80 by experimental studies, can be used to better characterise the deformation history of a rock  
81 and better constrain regional and global geodynamic models.

82

83 In contrast to pyroxenite layering in the mantle, the microstructures of pyroxene-rich  
84 intervals in lower-crustal mafic cumulates have received less attention from petrologists (e.g.  
85 Boorman et al., 2004; Feinberg et al., 2006; Higgins, 1998, 2015; Williams et al., 2006).  
86 More specifically, the crystallographic preferred orientation (CPO) of pyroxenes in crustal  
87 pyroxenites has not yet been investigated using electron backscatter diffraction (EBSD)  
88 methods (e.g. Prior et al., 1999; Wright et al., 2011). Pyroxenitic cumulates are mostly  
89 present in the lower-crustal section of ophiolites and in layered magmatic intrusions (e.g.

90 Benn and Allard, 1989; Cawthorn and Walraven, 1998; Ceuleneer and Le Sueur, 2008;  
91 Clénet et al., 2010; Ying et al., 2013).

92 In magmatic intrusions, the rocks can record both magmatic and deformational processes that  
93 generate preferred grain orientation. The difficulty when studying this kind of lithologies is to  
94 differentiate between the two processes, which could be overprinted by one another. Previous  
95 studies reported that the microstructure of cumulates may result from a sequence of processes  
96 including crystal nucleation, crystal settling and the subsequent compaction of the mush  
97 (Cheadle and Gee, 2017; McBirney and Nicolas, 1997; Nicolas, 1992). Fabric generated  
98 during magma flow aligns grains in a specific direction, thus conferring a planar-linear fabric  
99 on the rock, which then shows both a shape- and a crystallographic preferred orientation  
100 (CPO) (e.g. Boudreau and McBirney, 1997; Charlier et al., 2015; Namur et al., 2015 and  
101 references therein; Vukmanovic et al., 2018; Williams et al., 2006). In this case, olivine  
102 crystals are generally elongated on [001] and show a correspondence between (010) and  
103 macroscopic markers like layering and igneous foliation (e.g. Benn and Allard, 1989;  
104 Boudier, 1991). A similar behaviour has been reported for the crystallographic axis of  
105 clinopyroxenes (cpx) with their [001] axes clustering along the magmatic lineation, which is  
106 itself contained in the magmatic foliation coinciding with the (010) plane (e.g. Benn and  
107 Allard, 1989). During the subsequent magmatic history of the sample, the grains' SPO can be  
108 modified by late overgrowth that could change the primary fabric (e.g. Brothers, 1964;  
109 Cheadle and Gee, 2017). With decreasing proportions of melt, the deformation regime  
110 approaches the solid state and possible grain boundary sliding assisted by diffusion-  
111 precipitation processes at low stress will take place (e.g. Paterson, 2001). Finally, when the  
112 porosity becomes low enough, compaction occurs and tends to form a planar fabric; at this  
113 point the dominant deformation process becomes dislocation creep and leads to the formation  
114 of a CPO driven by plastic deformation .

115 Depending on the relative contribution of the processes involved, the respective strengths of  
116 the planar and linear component of the magmatic fabrics may vary. Consequently, the  
117 symmetry of the resulting fabric will range from an orthorhombic symmetry to a fibre  
118 symmetry (e.g. Benn and Allard, 1989; Biedermann et al., 2016; Feinberg et al., 2006). The  
119 symmetry of a magmatic fabric can thus be used as an indicator of the magmatic-flow  
120 geometry and can be related to magma-chamber processes (e.g. Higgins, 2015).

121 Unfortunately, in natural samples, it is common that the initial magmatic fabric is overprinted  
122 by a later event of solid-state flow. This overprint results in a new fabric that carries different  
123 information from the original magmatic fabric (e.g. Satsukawa et al., 2013).

124

125 In the Klamath Mountains, California (USA), the Trinity ophiolite crops out as a large  
126 peridotite body intruded by a dozen ultramafic-mafic plutons of sizes from a few km to 10  
127 km, exposed at different structural levels from the lower crust to the middle crust) Boudier et  
128 al., 1989; Cannat and Lécuyer, 1991; Ceuleneer and Le Sueur, 2008). Among them, the Bear  
129 Creek pluton exposes cumulates that crystallised in the vicinity of the mantle/crust boundary  
130 (Ceuleneer and Le Sueur, 2008). As the Trinity ophiolite did not experience extensive  
131 regional metamorphism after its formation, it provides a unique opportunity to study the  
132 macro- and microstructure of pyroxene-rich cumulates and to observe magmatic and  
133 deformational processes occurring in magma chambers in a supra-subduction zone. In this  
134 work, field observations and EBSD data are used to characterise the microstructure and CPO  
135 of cumulate minerals from the Bear Creek pluton and its host peridotite. This constitutes the  
136 first EBSD study of crustal pyroxenites from a magmatic intrusion. These results are then  
137 used to discuss the interplay of magmatic and deformational processes in the development of  
138 mineral fabric in this context.

139

## 140 2. Geological background

141

142 The Trinity ophiolite is the largest (3,000 km<sup>2</sup>) and best-preserved exposure of mantle mafic-  
143 ultramafic rocks cropping out in California. It is included in the Paleozoic Terranes accreted  
144 to the North American Cordillera during early Devonian times (e.g. Lindsley-Griffin, 1977).

145 Although its precise tectonic setting and emplacement history are poorly constrained, its  
146 association with arc-derived volcano-sedimentary formations together with geochemical and  
147 geochronological data suggest that it is a dismembered fragment of a former arc-related  
148 ocean basin that may have opened between Rodinia and Laurentia; the Trinity ophiolite  
149 itself could represent the youngest remnant of this oceanic domain (Brouxel et al., 1988;  
150 Coleman, 1986; Mankinen et al., 2002; Wallin et al., 1988; Wallin and Metcalf, 1998).

151

152 The Trinity ophiolite consists of an incomplete ophiolite sequence comprising mantle  
153 peridotites pockmarked by different plutons, which range from mafic-ultramafic to gabbroic  
154 and granodioritic in composition and several kilometres in size (Fig. 1A, Cannat and  
155 Lécuyer, 1991; Ceuleneer and Le Sueur, 2008). The mantle peridotites have a porphyroclastic  
156 texture that is typical of so-called mantle tectonites and that was developed under high  
157 temperature (close to the solidus) and low deviatoric stress, which have been attributed to  
158 asthenospheric flow (Le Sueur et al., 1984). An image of the flow geometry at the time it  
159 stopped was obtained by mapping the foliation and lineation imprinted by plastic  
160 deformation. The global survey of Le Sueur et al. (1984) revealed a rather organised pattern  
161 characterised by a sub-vertical foliation bearing a sub-horizontal stretching lineation, both  
162 trending NW-SE, i.e. oriented parallel to the inferred azimuth of the paleo-spreading axis.  
163 Local deviations from this regional pattern are frequent; some of them can be attributed to the  
164 development of late mylonitic shear zones.

165

166 The Trinity peridotites are mostly of lherzolitic composition and resulted from a moderate  
167 degree of decompression melting which started in the spinel lherzolite facies and ended in the  
168 plagioclase lherzolite facies (Quick, 1981). Patches of plagioclase lherzolite are quite  
169 represent about 10% of the surface of the Trinity peridotite (Quick, 1981). Local  
170 concentrations of plagioclase (+/- cpx and spinel) attest to melt migration and segregation  
171 contemporaneous with the end of plastic deformation (Ceuleneer and Le Sueur, 2008).

172

173 Abundant channels and dykes of pyroxenite (clinopyroxenite and cpx-rich websterites)  
174 crosscut the Trinity peridotites. The pyroxenites crystallised from a boninitic-andesitic melt  
175 (Mg / Si-rich and Ti-poor) derived from another mantle source that is not the Trinity  
176 lherzolite as presently exposed (Ceuleneer and Le Sueur, 2008). These boninitic-andesitic  
177 melts were in disequilibrium with the plagioclase lherzolite at low pressure as attested by the  
178 melt/rock reaction features exposed. Harzburgites and dunites crop out at the margins of the  
179 pyroxenite porous flow channels and dykes, to distances that can reach several meters  
180 (Dygert et al., 2016; Kelemen et al., 1992). Reactive dunite with minor harzburgite also  
181 occurs as bodies a few tens of meters thick and hundreds of meters in lateral extent. They  
182 have been called “tabular dunites” by Quick (1982) in reference to their shape and their  
183 subhorizontal orientation. The large compositional diversity of the Trinity peridotite at  
184 various scales can be ascribed to the cryptic effects of the interaction between the moderately  
185 depleted mantle lherzolite and the ultra-depleted melt that crystallised as pyroxenite dykes  
186 (Ceuleneer and Le Sueur, 2008). The overall tilt of the Trinity massif, at the regional scale,  
187 was found to be relatively moderate according to the orientation of the contacts between the  
188 different units making up the ophiolite and to the sub-vertical dip of the diabase dykes at  
189 upper-crustal levels (Le Sueur et al., 1984).

190

191 Among the plutons intrusive into the Trinity peridotite, granites and granodiorites were  
192 emplaced during Mesozoic times and are not related to the accretion history of the ophiolite.  
193 The mafic and ultramafic plutons are much older (405 to 435 Ma) (Wallin et al., 1995;  
194 Wallin and Metcalf, 1998) and their composition shows clear affinities with that of the  
195 pyroxenite dykes intruding into and reacting with the peridotite, which most likely belong to  
196 the same magmatic episode (Ceuleneer and Le Sueur, 2008). They are differentiated, with a  
197 lithological succession consistent with the classical ophiolite igneous stratigraphy i.e., from  
198 the base to the top, primitive layered cumulates, more evolved cumulates devoid of  
199 developed layering and diabase dykes interpreted as the root of a sheeted dyke complex that  
200 is not preserved due to erosion. Contrasting with the classical ophiolitic model, these crustal  
201 units present a limited lateral extent (a few km at most) and were emplaced at various depths  
202 within the peridotite (Cannat and Lécuyer, 1991; Wallin and Metcalf, 1998).

203

204 The Bear Creek area exposes the most complete and continuous section through one of these  
205 mafic and ultramafic plutons (Ceuleneer and Le Sueur, 2008). Its lower contact with the  
206 mantle-derived rocks (i.e. of lherzolitic composition) is affected by a late fault where the  
207 Trinity River flows (Fig. 1B). The lateral contact with the host rock is underlined by a screen  
208 of pegmatite made up essentially of large crystals of cpx (up to a few decimetres in length)  
209 partly replaced by magmatic hornblende and lower-temperature alteration minerals. In the  
210 pluton, the basal cumulate section is ~500 m thick and comprises an alternation of cm-thick  
211 layers of quite variable composition (dunite, wehrlite, pyroxenite, lherzolite...). Plagioclase  
212 is typically absent from this horizon; the modal abundance of olivine gradually decreases  
213 from bottom to top and it is virtually absent from the uppermost part of the cumulate pile.  
214 Plagioclase appears above this ultramafic sequence, in the upper half of the cumulate section,

215 in a diffuse way at first (plagioclase pyroxenites), becoming increasingly abundant toward the  
216 top of the section. Its crystallisation always coincides with that of hornblende. The top of the  
217 cumulate sequence is characterised by abundant magmatic breccias crosscut by diabase  
218 dykes, and is not shown in Fig. 1B (Le Sueur et al., 1984).

219

220 Ceuleneer and Le Sueur (2008) attributed the aforementioned crystallisation sequence and the  
221 bottom-to-top evolution in modal and mineral compositions to the intrusion of a single batch  
222 of boninitic-andesitic melt (high MgO, silica and water content, low Al<sub>2</sub>O<sub>3</sub> and low TiO<sub>2</sub>)  
223 into the Trinity peridotites in a supra-subduction setting. Furthermore, the occurrence of  
224 diabase dykes at the top of the cumulate sequence were interpreted as representing the roots  
225 of a sheeted dyke complex and suggests that the magma injection occurred at relatively low  
226 pressure ( $\ll 1$  GPa) in a spreading setting (Le Sueur et al., 1984).

227

### 228 **3. Field observations**

229

230 In the Bear Creek plutonic section, the basal level (~500 m thick) is made up of serpentinised  
231 dunite layers alternating with pyroxene-rich and serpentine-free layers varying in  
232 composition between websterites, wehrlites and lherzolites. The thickness of these layers  
233 ranges from several hundred micrometres (i.e. similar to the grain size) to several  
234 centimetres. We will refer to this compositional alternation between dunite and pyroxene-rich  
235 layers as “finely layered cumulates” (Figs. 2, 3A, 3B and Ceuleneer and Le Sueur, 2008).

236 The compositional layering is marked and is the unique macroscopic structural feature visible  
237 in the field. Its strike ranges from N115° to N85° with an associated dip of 30° to 40°S. The  
238 lateral extent of the layers exceeds several tens of metres and oblique structures made of  
239 clinopyroxenitic intrusions, generally with a coarser-grained texture, were observed.

240 Peridotitic enclaves and pyroxene megacrysts (e.g. sample T3BC3A, Ceuleneer and Le  
241 Sueur, 2008) also occur throughout this cumulate lower section, locally interrupting the  
242 compositional layering (i.e. at the hand specimen scale and thin section scale respectively;  
243 Supplementary Material B).

244 Towards higher stratigraphic levels, the compositional layering becomes increasingly  
245 difficult to observe due to the progressive disappearance of olivine-rich layers (Figs. 1B and  
246 3E). This results in seemingly more massive layers (up to ~250 m thick) that display a  
247 variable but always high cpx / orthopyroxene (opx) ratio and that we will refer to as "massive  
248 cumulates" (Fig. 3C and D). The strike of the layering, where still measurable, remains in the  
249 same range as that of the finely layered cumulates but its dip is more variable, ranging from  
250 60 to 20°S.

251

252 The country rock in which the cumulates are embedded is of lherzolitic composition (Figs.  
253 2A, 3E and 3F). The lherzolite is highly serpentinitised and contains relatively fresher  
254 subparallel 1-5 cm thick pyroxenite veins highlighting a foliation which is also visible thanks  
255 to pyroxene grains (Fig. 3E). The foliation of the lherzolites ranges between N115° and N45°  
256 30-40°S. In contrast to the cumulates, a mineral elongation was identified in the lherzolite  
257 and remains sub-horizontal. Figure 2A shows the contact between the lherzolite and the  
258 finely layered cumulates which is unfortunately always hidden by loose blocks. A clear  
259 contact between the finely layered cumulates and the lherzolite foliation was only observed  
260 on a loose block, and was discordant. It is noteworthy that we did not observe any plagioclase  
261 within the Bear Creek finely layered cumulates or lherzolite.

262

263 In some locations along the section that we sampled, clinopyroxenite sills and dykes locally  
264 crosscut both the lherzolite foliation and the compositional layering of the cumulates (Fig. 3A

265 and 3E). They appear to be dendritic extensions of meter-scale pockets of clinopyroxenitic  
266 intrusions that crop out locally in the lherzolite. The clinopyroxenitic dikes and sills can  
267 exhibit (1) a pegmatitic texture with idiomorphic, centimetric grains or (2) a finer-grained  
268 texture comparable to that of the massive cumulates. The two textures can coexist within a  
269 single clinopyroxenite intrusion with the pegmatitic texture making up the core of the dyke  
270 and the finer-grained texture appearing at the rim.

271

272

## 273 **4. Sample collection and analytical methods**

274

### 275 **4.1. Sample collection and preparation**

276

277 Our sampling of the Bear Creek intrusion and its host rock covers a range of lithologies  
278 including the host mantle section (i.e. lherzolite) and the finely layered and massive  
279 cumulates that crop out in the basal section of the intrusion. At Bear Creek, sampling was  
280 done along a section roughly perpendicular to the compositional layering of the cumulates  
281 (Fig. 1B and Tab. 1). Two lherzolites, ten finely layered pyroxene-rich cumulates, two  
282 massive pyroxenites and two clinopyroxenitic sills were selected for microstructural  
283 characterisation by EBSD. The samples are described in detail in Table 1 and Supplementary  
284 Material A, including GPS coordinates and microstructural data.

285

286 For samples in which no lineation could be observed in the field nor during sample  
287 preparation, thin sections were systematically cut in the plane normal to the foliation and  
288 containing the N115° direction. This direction corresponds to the azimuth of the regional  
289 stretching elongation in the mantle peridotites and to the strike of the intrusive diabase dykes,

290 as inferred from the structural studies of Le Sueur et al. (1984) and Boudier et al. (1989).  
291 This direction was eventually used to relate the microstructure of the cumulate with that of  
292 the neighbouring peridotites. A suite of samples (i.e. 01T12A, 01T13A, 01T13B, 01T13C,  
293 03T46B and 02T117A) collected in a previous field expedition was cut perpendicular to the  
294 compositional layering but was not oriented relative to the Trinity structural framework. For  
295 all samples, mineral fabrics were interpreted after checking the coincidence of the azimuth of  
296 the crystallographic-axis directions of at least two phases; petrofabrics were not interpreted  
297 where this criterion of internal consistency could not be verified.

298

## 299 **4.2. Analytical methods**

300

301 During sample preparation, a colloidal silica-water solution (mixed in a 70:30 proportion)  
302 was used for 5 min following mechanical polishing, in order to reduce surface damage. Thin  
303 sections were then coated with a ~ 6-nm-thick carbon layer to prevent charging during  
304 analysis. Crystallographic orientations of minerals were acquired using an HKL NordlysNano  
305 EBSD detector attached to a Zeiss EVO MA15 scanning electron microscope in the  
306 Geochemical Analysis Unit (GAU) at GEMOC/CCFS, Macquarie University, Australia. For  
307 all analyses, a 15- $\mu\text{m}$  step size and a 20-kV acceleration voltage were used; working distance  
308 ranged between 15 and 20 mm. Automatic indexing was performed using the AZtec software  
309 (Oxford Instruments). The HKL software was used to perform a standard noise reduction and  
310 to extrapolate missing data with at least 8, 7, 6 and then 5 identical neighbours. Resulting  
311 EBSD data were then processed in MATLAB using the MTEX toolbox (Bachmann et al.,  
312 2010b, 2011). A value of  $10^\circ$  as the cut-off angle for the determination of the grains was  
313 used. Further details on the data processing protocol in MTEX can be found in Henry et al.  
314 (2017) and Henry (2018).

315

316 To avoid oversampling of large grains, pole figures were plotted with one point per grain on a  
317 lower-hemisphere, equal-area stereographic projection. For strongly serpentinised samples (3  
318 samples), pole figures were produced using available measurements, which proved to yield  
319 results comparable to those of a standard one-point-per-grain model (Achenbach et al., 2011)  
320 (see Supplementary material A for the number of grains and the type of representation).

321 When twinning in cpx was detected during data processing, pole figures of cpx were drawn  
322 using all the available measurements.

323

324 Orientation density functions (ODF) have been calculated with a  $10^\circ$  Gaussian half-width for  
325 samples with  $> 100$  grains/individual measurements. The strength of the crystallographic  
326 preferred orientation was estimated using both the J- and M-indices (Bunge, 1982; Skemer et  
327 al., 2005) and the appropriate ODF (i.e. calculated after all the measurements if twinning or  
328 serpentinisation occurred otherwise using one point per grain). In addition, the misorientation  
329 of each pixel was calculated relative to the mean orientation of its corresponding grain, and  
330 then combined as maps of misorientation relative to mean grain orientation. Any  
331 misorientation value greater than  $10^\circ$  away from the mean orientation was equated to  $10^\circ$  to  
332 allow for a clearer observation. Orientation tensors were also calculated for each  
333 crystallographic axis of each phase of interest using the method of Bachmann et al. (2010a).  
334 For each orientation tensor, eigenvalues for [100], [010] and [001] of olivine, cpx and opx  
335 were extracted and used to quantitatively describe the fabric symmetry using the BA- and  
336 LS-indices (Mainprice et al., 2015; Ulrich and Mainprice, 2005). In order to quantify a  
337 possible shape-preferred orientation (SPO) of the grains that may not have been obvious in  
338 thin section, we used EBSD data to quantify their shape. To do so, we fitted an ellipse on  
339 every grain and extracted the angle between the long axis of that ellipse and the X direction

340 (i.e. N115 direction in the layering plane). Results are then plotted as a multiple rose diagram  
341 with each data point being weighted by the surface area of the grain.

342

## 343 **5. Petrography and microstructures of the Bear Creek intrusion and its country rocks**

344

### 345 **5.1. Lherzolitic country rock**

346

347 The lherzolites are highly serpentinitised, mostly preserving opx porphyroclasts (~ 2 mm),  
348 which are surrounded by fine-grained (~50 µm) olivine and minor cpx (Fig. 3F, samples  
349 T4BC2 and T4BC3). Undulose extinction, sub-grain boundaries and cpx exsolution along  
350 cleavages are observed in the large grains. Olivine is coarse-grained (~3 mm) away from  
351 opx-rich aggregates, and free from observable deformation markers. No obvious shape-  
352 preferred orientation of the grains is visible in thin section.

353

### 354 **5.2. Finely layered cumulates**

355

356 In some of our samples (e.g. T3BC1A, Fig. 3B, 4A and Table 1), olivine, opx and cpx are  
357 relatively homogeneously distributed. However, in other samples high-frequency alternation  
358 between olivine-rich and pyroxene-rich millimetre-thick layers is visible (Fig. 4B and 4C).  
359 The transition between layers is sharp and no gradual change in the mode of olivine is seen.  
360 Mineral modes can vary strongly within each compositional layer, within the sample and  
361 from one sample to the others (Fig. 4 and Ceuleneer and Le Sueur, 2008). Grain-size  
362 distribution is rather homogeneous with a mean of ~ 400 µm for all phases. Grain boundaries  
363 between phases are curved/lobate and 120° contacts are common. Grain boundaries can be  
364 either straight or curvilinear between grains of same phase and 120° triple junctions are

365 common. We did not preferentially observe either convex or concave grain boundaries of a  
366 specific phase at contacts between two phases. Some olivine and cpx grains can be elongated  
367 on the layering plane but no clear shape-preferred orientation is seen for any phase. Only rare  
368 deformation markers can be observed in the finely layered cumulates (i.e. straight sub-grain  
369 boundaries in olivine, and to a lesser extent in cpx and opx; Fig. 5A). Cpx often presents  
370 twins with continuous to stepped twin-boundaries crosscutting the whole grain in most cases.  
371 At the thin section scale, macrocrysts of opx (~ 1 cm) can bend the layer contacts and can  
372 cross over multiple layers (e.g. T3BC3A, Supplementary Material B). Amphibole appears as  
373 small interstitial grains (~150  $\mu\text{m}$ ), often associated with cpx. An amphibole-rich vein  
374 crosscutting the cumulates was observed in sample 01T13A (Fig. 4C).

375

### 376 **5.3. Massive cumulates**

377

378 In contrast to the finely layered cumulates, this lithology is dominated by coarse-grained  
379 minerals (~ 500  $\mu\text{m}$  to 1 mm) made up essentially of cpx alternating with rare olivine with  
380 minor opx (i.e. compositional layering visible in the field, Fig. 3E). Cpx grain boundaries are  
381 mostly lobate, but can also be locally straight (i.e. Fig 5B). In the finer-grained fraction (~ 50  
382  $\mu\text{m}$  grain size, <5% of the sample surface area), olivine and opx assemblages appear with  
383 mainly lobate/curved grain boundaries. Triple junctions are visible between most cpx grains  
384 and indicate a local textural equilibrium. Internal deformation in the form of subgrains and  
385 undulose extinction is observed in olivine, and sometimes in cpx grains. EBSD-derived maps  
386 reveal that concentric misorientation is present in some cpx grains (Fig. 5B). As in the finely  
387 layered cumulates, cpx macrocrysts (~ 1 cm) locally occur and twinned cpx are also observed  
388 (sample T4BC4A, Supplementary Material B).

389

#### 390 **5.4. Shape-preferred orientation of the Bear Creek cumulates**

391

392 The shape-preferred orientation (SPO) of the grains in the Bear Creek cumulates was  
393 investigated by EBSD mapping. In the finely layered cumulates, our results show a clear  
394 elongation of the cpx and olivine grains in the layering plane (Fig. 6A). Opx present an SPO  
395 with a preferred direction of elongation normal to the layering plane.

396 In the massive cumulates, the quantification of cpx SPO shows a range of orientations from  
397 sub-parallel to olivine and cpx in the finely layered cumulate (sub-parallel to N115 direction)  
398 to a maximum at a small angle to the lineation (Fig. 6B).

399

#### 400 **5.5. Clinopyroxenite intrusions**

401

402 Clinopyroxenite intrusions are composed dominantly of sub-idiomorphic to idiomorphic  
403 coarse-grained cpx (ranging in size from ~5mm to ~2 cm, Fig. 7) with interstitial  
404 assemblages of olivine, cpx, opx and hornblende (1-5 mm). Grain boundaries appear linear  
405 and 120° triple junctions are common among cpx grains. Rare macrocrysts of euhedral to  
406 subhedral cpx locally exhibit twinning with straight to stepped twin boundaries (Fig. 7B, 7C  
407 and Ceuleneer and Le Sueur, 2008). In contrast, olivine and opx are xenomorphic, with  
408 mostly lobate or curvilinear grain boundaries; triple junctions and deformation markers are  
409 absent. Locally, these intrusions grade into finer-grained layers (e.g. sample 02T117-A)  
410 where their texture becomes similar to that of the massive cumulates (Figs. 7A and 8A).

411

### 412 **6. EBSD results**

413

#### 414 **6.1. Lherzolithic country rock**

415

416 The mineral fabrics of olivine, cpx and opx from the two analysed lherzolites are presented in  
417 Fig. 9. The olivine fabric shows a strong concentration of [010] axes perpendicular to the  
418 foliation plane, while either [100] or [001] axes are sub-parallel with the lineation direction  
419 depending on the sample. The cpx fabric has [001] axes parallel to the lineation and [010]  
420 axes perpendicular to the foliation plane. Opx exhibits a cluster of [001] axes around the  
421 lineation direction and a weak point maximum for [100] and [010] axes, both fitting the  
422 foliation pole (Fig. 9). Amphibole, when present, has a fabric mimicking that of cpx  
423 (Supplementary Material D). The fabric symmetry for olivine and opx in the lherzolite plots  
424 within the orthorhombic domain while cpx is spread between the orthorhombic and planar  
425 domains (Fig. 10).

426

## 427 **6.2. Finely layered cumulates**

428

429 The finely layered cumulates were investigated using nine samples; results are shown in  
430 figure 11 (see also Figs. 4, 5A and Table 1). The grain sizes calculated using EBSD data do  
431 not show any variation across this part of the section (Supplementary Material C). The  
432 olivine aspect ratio is always slightly higher than that of the pyroxenes, for a smaller grain  
433 size. The olivine fabric is dominated by a strong concentration of [010] axes perpendicular to  
434 the layering plane. Olivine [100] and [001] axes are distributed as girdles in the layering  
435 plane (Fig. 10). This observation is consistent with the BA-indices (Fig. 10), suggesting  
436 [010]-axial symmetries for the olivine fabrics. Other samples exhibit clustering of the [001]  
437 axes (e.g. samples T4BC7B, 01T12A) or the [100] axes (e.g. samples T3BC3A and 01T13A,  
438 Fig. 11) around the N115° direction. Cpx displays a clustering of [010] axes, and to a lesser  
439 extent of [100], normal to the layering plane. The cpx [001] axes mostly form girdles in the

440 layering plane, as indicated by their low LS-indices (Fig. 10, Sup. Material A), but may also  
441 define a sub-maximum within the girdle, close to the N115° direction. Cpx fabrics are  
442 dominated by a planar symmetry, as again indicated by their low LS-indices (Fig. 10). The  
443 opx fabric usually has a weak concentration of both [100] and [010] axes next to the layering  
444 pole, while the [001] axis forms a girdle with a sub-maximum aligned in the N115° direction  
445 (Fig. 11). Orientation maps reveal that two evenly-spread populations of opx may coexist and  
446 are responsible for the [100] and [010] clusters near the pole of the layering plane  
447 (Supplementary Material B). Opx appears to have higher BA-indices than LS-indices,  
448 suggesting a greater contribution of [010] and [001] of opx to the planar structure (Figs. 10  
449 and 11). When amphibole is present, its fabric is similar to that of cpx (Fig. 10). As described  
450 earlier, a thin amphibole vein crosscutting the magmatic layering is observed in one sample  
451 (01T13A, Fig. 4C). The fabric of the amphibole making up the vein is similar to that of the  
452 amphibole in the finely layered cumulates that appears as interstitial grains between olivine,  
453 opx and cpx grains. Twinning of the cpx in the finely layered cumulates is characterised by  
454 EBSD and represents a rotation of about 180° around [001].

455

### 456 **6.3. Massive cumulates**

457

458 Two samples (T3BC4A, T4BC4A) were used to investigate the fabric of massive cumulates  
459 (Fig. 12). In both samples, the cpx [010] axes form a cluster normal to the layering plane  
460 while [001] axes are scattered and form a girdle in the layering plane (Fig. 12). In sample  
461 T3BC4A, olivine yields a fabric with the [001] axes clustering weakly along the N115°  
462 direction and the [010] axis normal to the layering. The number of olivine grains in sample  
463 T4BC4A does not allow for a clear interpretation of the fabric. In terms of fabric symmetry,  
464 cpx in our two samples has a low LS-index, suggesting a strong planar component for the

465 fabric, while the only occurrence of olivine plots in the orthorhombic domain (Fig. 10). In the  
466 massive cumulates, the occurrence of opx and amphibole is so low that no reliable  
467 observation of the mineral fabric can be made.

468

#### 469 **6.4. Clinopyroxenitic intrusions**

470

471 The pegmatitic microstructure in the clinopyroxenitic intrusions was investigated using  
472 sample 03T16A (Figs. 7B and 7C, Supplementary mat. E). The determination of fabrics is  
473 hampered by the lack of structural framework inherent to this lithology; internal deformation  
474 is lacking, and the large grain-size limits the number that can be analysed. In sample  
475 03T16A, cpx and amphibole are the only phases with sufficient grains to calculate an ODF.  
476 The cpx [001] axes exhibit point maxima for sample 03T16A (Supplementary mat. E). In  
477 sample 03T16A, amphibole displays a fabric similar to that for cpx.

478

479 The microstructure of the finer-grained section of the clinopyroxenite intrusion was studied  
480 in sample 02T117-A, which represents the contact between a clinopyroxenitic intrusion and  
481 the finely layered cumulates (Fig. 8A, B). In the clinopyroxenite part, only cpx was observed  
482 while cpx, opx and olivine are all visible in the finely layered cumulates. The cpx in the  
483 clinopyroxenite intrusion shows [010] normal to the intrusion plane with [001] axes forming  
484 a girdle on that plane. The fabrics and textures observed in the finely layered cumulate are  
485 comparable to that previously described. Similarly, the amphibole fabric matches that of cpx  
486 (Supplementary mat. E).

487

488

#### 489 **7. Discussion**

490 Field observations, textural and microstructural data are integrated from the bottom to the top  
491 of the Bear Creek intrusion and its associated mantle domain in order to unravel the solid  
492 state and magmatic processes that took place in the Bear Creek. Implications of the  
493 deformation episodes and the related conditions are then considered in the context of the  
494 evolution of the Trinity ophiolite.

495

### 496 **7.1. Conditions of deformation in the host Trinity mantle**

497

498 In this section, we first discuss the EBSD data in the light of the field and microstructural  
499 observations and then use them to estimate the conditions under which plastic deformation  
500 occurred prior to the intrusion.

501

502 Lherzolitic cpx displays a SL-type fabric ([010] and [001] axes of clustering along the  
503 foliation pole and the lineation direction respectively), suggesting deformation at high  
504 temperature, and a combination of pure and simple shear (Bascou et al., 2002; Helmstaedt et  
505 al., 1972). Opx displays a ABC fabric (i.e. [001] axis along the lineation direction and weak  
506 cluster of [100] and [010] normal to the layering, Jung et al., 2010) while olivine shows an A-  
507 type fabric (T4BC2A), consistent with deformation of the lherzolite by dislocation creep at  
508 high temperature and low stress under “asthenospheric” conditions in the upper mantle (Jung  
509 and Karato, 2001; Michibayashi and Oohara, 2013). Sample T4BC3A (Figs. 3E and 9) was  
510 collected less than 2 m below the finely layered cumulates of the Bear Creek intrusion in the  
511 cross section and is the closest lherzolite sample to the contact between the intrusion and the  
512 host rock. The olivine fabric can be interpreted as a [001](010) (B-type, Jung and Karato,  
513 2001). We suggest that the possible change in the olivine fabrics between A- and B-type  
514 could be related to ongoing plastic deformation conditioned by infiltration of melt from the

515 intrusion, which could trigger a fabric switch either by the integration of structural water *via*  
516 diffusion and /or the presence of interstitial melt (Jung and Karato, 2001; Kohlstedt and  
517 Holtzman, 2009; Qi et al., 2018).

518

## 519 **7.2 Magmatic and plastic processes recorded in the Bear Creek intrusion**

520

521 Ceuleneer and Le Sueur (2008), based on the igneous stratigraphy, proposed that the Bear  
522 Creek intrusion evolved in a closed system following the injection of a single batch of  
523 magma in the shallow lithosphere. Studying the microstructure of cumulates could thus  
524 potentially provide valuable information on the dynamics of crystallisation and direction of  
525 transport in this specific magmatic environment. Below, we decipher the progression of the  
526 deformation in the section.

527

### 528 **7.2.1. Constraints from the finely layered cumulates**

529

530 At the base of the cumulate section, our field observations revealed that the finely layered  
531 cumulates display a well-defined planar structure corresponding to the compositional  
532 layering (Fig. 2). On the layering plane, no lineation or foliation (i.e. crystal shape-preferred  
533 orientation) were visible at the outcrop or hand specimen scale. In the finely layered cumulate  
534 microstructure, we observed the occurrence of growth twins in cpx. The quantification of  
535 mineral SPOs shows that the long axis of the larger population of grains of olivine and cpx  
536 are subparallel to N°115, while opx grains are preferentially aligned at about 90 degrees to  
537 cpx and olivine (i.e. subparallel to the layering pole, Fig. 6A). The orthogonal shape-  
538 preferred orientation of opx relative to the orientation of cpx and olivine (note the slight  
539 elongation of opx in Fig. 4B), and very scarce internal deformation (Fig. 5A) are not

540 consistent with extensive plastic deformation. All the above suggest that the macro- and  
541 microstructures of the finely layered cumulates were not overprinted by extensive plastic  
542 deformation and probably preserve magmatic features. Regarding the mineral fabrics, olivine,  
543 opx and cpx CPOs have [001] axes forming girdles on the compositional layering. This has  
544 been observed in a magmatic context (e.g. Holness et al., 2017) and is consistent with the  
545 preservation of magmatic features in the finely layered cumulates that was hinted at by field  
546 and microstructural observations.

547

548 Although no macroscopic lineation was detected, opx, cpx [001] and ol [001] or [100]  
549 crystallographic axes define sub-maxima aligned along the regional N°115 orientation, which  
550 is also the stretching lineation in the mantle peridotites (Fig 11). Le Sueur et al. (1984) and  
551 Boudier et al. (1989) interpreted this lineation in the peridotite as reflecting asthenospheric  
552 flow channelised parallel to the azimuth of the former spreading centre. The olivine and  
553 pyroxene clusters can have two origins. (1) Formed through mechanical alignment of crystals  
554 by rotation around the vorticity axis of minerals during magmatic flow, when the proportion  
555 of melt is still high or (2) formed by limited plastic deformation at low melt volume probably  
556 driven by the regional stress field in the case of the Bear Creek intrusion (Boudier et al.,  
557 1989; Le Sueur et al., 1984). The limited evidence of plastic deformation reported here, such  
558 as the few subgrains and undulose extinction in olivine, cpx and opx (Fig. 5A) could be  
559 linked to plastic deformation under low stress (i.e. regional stress) or alternatively could be  
560 the result of the compaction process.

561 We suggest that the texture and CPO observed in the finely layered cumulates may have been  
562 formed by the following processes. (1) Rock-forming minerals crystallising with a shape  
563 anisotropy would be deposited and a preferred orientation was induced by a moderate  
564 magmatic flow; (2) compaction of the cumulates leading to limited plastic deformation and to

565 the accentuation of the planar feature together with a reduction of the linear feature (Figs. 2A,  
566 4, 6 and 11). Alternatively, an additional and limited episode of deformation could have  
567 occurred and could have been responsible for the weak clusters of [001] in pyroxenes and  
568 olivine contained in the girdles.

569

570 If an initial shape anisotropy was present during crystal settling, our results suggest that cpx  
571 crystals are likely to settle mainly on the (010) plane, and to a minor extent on the (100)  
572 plane. In EBSD-derived orientation maps, we observe two populations of opx SPO. The first  
573 population displays a long axis contained in the compositional plane and has the [010] axis  
574 parallel to the layering plane pole. The second population has a long axis perpendicular to the  
575 layering plane and has the [001] axis parallel to the layering pole (Supplementary Material  
576 B). Based on these observations, we suggest that (010) is more likely to be the settling plane  
577 for opx than (100) as (010) and the crystal long axis are contained within the compositional-  
578 layering plane. In Bear Creek, olivine crystals tended to preferentially settle on the (010)  
579 plane. For all three minerals, the [001] axis commonly is within the layering plane, consistent  
580 with the fact that this axis coincides with the direction of crystal elongation.

581

582 These results are consistent with previously-reported fabrics in layered intrusions from the  
583 crustal section of the Oman ophiolite. (Benn and Allard, 1989) showed that the (010) planes  
584 of olivine and cpx coincide with the compositional layering. Similar observations were made  
585 in recent studies of layered intrusions from different geological settings (e.g. Holness et al.,  
586 2012; Vukmanovic et al., 2018). Our observations are also consistent with recent modelling  
587 and the study of adcumulates from a mafic-ultramafic intrusion in the Tarim Craton, which  
588 showed that compaction can lead to weak B-type fabrics and formation of subgrains in  
589 olivine (Yao et al., 2019).

590

### 591 **7.2.2. Constraints from the massive cumulates**

592

593 In a previous study of the Bear Creek intrusion, Ceuleneer and Le Sueur (2008) used the  
594 continuous gradational lithological change and the continuous and correlated variations in  
595 major elements (i.e. Mg#) to interpret the finely layered cumulates and the massive cumulates  
596 as the crystallisation product of a single crystallisation sequence. The massive cumulates are  
597 essentially mono- to bi-mineralic in the olivine-poor level, and exhibit a coarser grain size  
598 and straighter grain boundaries than the finely layered cumulates (Figs. 3D and 5B). Our  
599 results show that the fabrics observed in the massive cumulates with development of girdles  
600 on pyroxene [001] axes are comparable to those of their finely layered counterparts (Fig. 12).  
601 The fabric of olivine in the massive cumulates plots into the orthorhombic symmetry (Fig.  
602 10) and contrasts with that of cpx. Based on the change in fabric symmetry and the likely  
603 preservation of magmatic microstructures in the cpx-rich layers, we suggest that the olivine-  
604 rich layers may have preferentially recorded and accommodated any deformation subsequent  
605 to the magmatic stage (i.e. compaction or solid state deformation). The quantification of cpx  
606 SPO shows a range of orientations from sub-parallel to olivine and cpx in the finely layered  
607 cumulates (parallel to the lineation) to a maximum at small angle to the lineation (Fig. 6).  
608 This fan of orientations could be due to the nearly monomineralic composition of the layer  
609 triggering further crystal growth.

610 The lack of deformation markers observed during the field investigation, the relatively scarce  
611 internal deformation of large cpx crystals (Fig. 5B), and the CPO of cpx showing a girdle on  
612 [001] with weak clusters (Fig. 12) mimic what was observed in the finely layered cumulates  
613 (Fig. 5A and 11). Considering the above and the concentric subgrain boundaries observed in  
614 the cpx in the massive cumulates, our data suggest that the microstructure of the massive

615 cumulates is mostly magmatic. A similar combination of processes was at play in the finely  
616 layered cumulates. This includes a weak magmatic flow and a limited episode of plastic  
617 deformation (probably due to compaction or to regional stress). In this case, the coarser cpx  
618 grain size and straighter grain boundaries in the massive pyroxenites can be interpreted as a  
619 combined consequence of the rock composition and the crystallisation processes. The  
620 crystallisation of a single liquidus phase would favour growth of early grains (rather than  
621 high nucleation rate), possibly by grain-boundary migration at high temperature, as suggested  
622 by the complex grain-boundary shapes of some grains in the massive pyroxenites (e.g. Fig.  
623 5B). Conversely, in the finely layered cumulates, the homogeneous distribution of the phases  
624 will result in a smaller grain-size and can satisfactorily account for the curvilinear grain  
625 boundaries at the contact between different phases (Figs. 3 and 5).

626

### 627 **7.2.3. Constraints from the clinopyroxenitic intrusions**

628

629 Clinopyroxenite intrusions cross-cut the layered pyroxenitic cumulates (Fig. 3A and 3C), and  
630 have a pegmatitic texture (i.e. grain size from 1 mm to multiple centimetres). The grain size  
631 of the clinopyroxenitic intrusions can decrease towards the rims of the dykes and may  
632 approach the grain size of the host cumulate layers. This can make such intrusions difficult to  
633 distinguish from the massive pyroxenites. The presence of numerous cpx twins (Fig. 7B and  
634 7C) and the low internal deformation suggest a purely magmatic origin for their  
635 microstructure. However, and contrary to the finely layered cumulates and massive  
636 cumulates, the relatively small size (~ 5-10 cm) of the clinopyroxenitic intrusions does not  
637 allow compaction and crystal settling to operate. The textures and fabrics observed in the  
638 sample of a clinopyroxenitic intrusion that preserves the contact with finely layered  
639 cumulates (02T117-1; Fig. 8A and 8B) are indistinguishable from those observed in the

640 massive pyroxenites (Fig. 5B and 12). In the finer-grained part of the clinopyroxenitic  
641 intrusions ( i.e. part shown in Fig 8), epitaxial crystallisation of new cpx grains on the cpx  
642 already present in the finely layered cumulates or massive pyroxenites can explain the  
643 development of the observed fabric. In the pegmatitic parts of the clinopyroxenitic intrusions  
644 (sample 03T16B, Fig. 7B, 7C and Supplementary Material E), the orthorhombic symmetry of  
645 the cpx fabric could be interpreted as a clue to a magmatic flow geometry within the dyke,  
646 which would not be purely linear. However, the presence of twined cpx leads to an over-  
647 sampling of the large grains during data collection, thus creating an impression of  
648 orthorhombic symmetry while the actual symmetry could be linear (which would be expected  
649 within a dyke). Although further investigation is required (in particular, analysis of their  
650 respective chemical compositions), it cannot be excluded that some intrusions and massive  
651 pyroxenites could be cogenetic, especially in sections where no olivine-rich levels are visible.

652

653

#### 654 **7.2.4. Amphibole in the Bear Creek**

655

656 Small amounts of igneous amphiboles (brown hornblende and pargasite) occur in every  
657 lithology from the Bear Creek area (Tab. 1). Amphibole is usually found as interstitial grains  
658 (Fig. 4), is commonly associated with cpx and can also appear as veins discordant to the  
659 layering (01T13A, Fig. 4C). In our samples, the amphibole CPO systematically mimics that  
660 of the cpx (i.e. [001](010)). This fabric contrasts with the previously-reported dislocation-  
661 creep-induced fabrics in amphibole (e.g. Ko and Jung, 2015). The observation that an  
662 amphibole-rich vein cross-cutting the pre-existing layering (Fig. 4C) shows a CPO similar to  
663 that of disseminated amphiboles within the sample (Fig. 11 and Supplementary Material E) is  
664 an indication of a possible melt/rock or fluid/rock-interaction origin for the amphiboles in

665 Trinity. The textural relationship between cpx and amphibole, together with the mimicking of  
666 the crystallographic preferred orientations of cpx by the amphibole, also point to a possible  
667 epitaxial growth of the amphibole as already observed in other localities (e.g. Henry et al.,  
668 2017; Kaczmarek et al., 2016; Moghadam et al., 2020).

669

### 670 **7.3. A scenario for the emplacement of the Bear Creek intrusion**

671

672 The magmatic processes and the plastic deformation recorded in the Bear Creek intrusion  
673 share similarities with other intrusions emplaced in extensional settings (e.g. Holness et al.,  
674 2012; Holness et al., 2017; Vukmanovic et al., 2018 and reference therein). However, the  
675 Bear Creek intrusion presents some features that could be typical for this type of  
676 environment, and lead us to draw a scenario for its emplacement into the mantle domain  
677 exposed in the ophiolites.

678

679 (1) An episode of solid-state flow occurred in ambient Trinity mantle wall-rock, mostly  
680 under high-temperature and low-stress conditions in the dislocation creep regime. This  
681 episode probably occurred as the “asthenospheric” mantle rose in an oceanic spreading  
682 environment and was channelised at shallow depth along the spreading axis (e.g.  
683 Boudier et al., 1989; Dygert et al., 2016; Le Sueur et al., 1984). Pressure probably was  
684 below 1 GPa (Quick, 1981) and the temperature above 1000°C so that an A-type olivine  
685 fabric could form as observed in the Iherzolite.

686 (2) In the Bear Creek area, intrusion of a boninitic magma at shallow depth (<1 GPa) led to  
687 the crystallisation of opx, cpx and olivine, producing finely layered cumulates, then with  
688 further differentiation, massive pyroxenites dominated by cpx (Ceuleneer and Le Sueur,  
689 2008). During that accumulation of ultramafic minerals, a dominantly planar mineral

690 fabric developed in the cumulates due to the combination of a crystal settling with weak  
691 magmatic flux. With decreasing melt proportions, compaction probably operated; it  
692 could have accentuated the planar component of the lithologies and formed the  
693 subgrains observed in the minerals of the Bear Creek samples. In the fabrics, we  
694 observe the presence of sub-maxima of preferred orientation for cpx, opx or olivine  
695 crystallographic axes within girdles coinciding with the compositional layering (Fig. 9).  
696 This may provide constraints on the geometry of the magmatic flow in a magma-  
697 chamber setting, and/or it may reflect the persistence of the regional stress field. Our  
698 observations suggest that the magmatic processes recorded are homogeneous over the  
699 entire section. Later intrusions occurred, crystallising into coarse-grained to pegmatitic  
700 clinopyroxenite-rich veins and dykes crosscutting the weakly-consolidated cumulate  
701 layers. Finally, the crystallisation of amphibole was followed by epitaxial growth on  
702 cpx.

703

## 704 **8. Conclusions**

705

706 New field and EBSD data have allowed us to characterise the deformation mechanisms and  
707 the formation/deformation history of the layered pyroxenitic cumulates, and their  
708 relationships with the host mantle peridotites (Iherzolite) in the Trinity ophiolite. This  
709 detailed microstructural study of the Bear creek intrusion suggests a scenario for the  
710 formation of layered intrusions that first includes crystal settling, then magma flow and later  
711 compaction. CPO, SPO and internal deformation of minerals suggest that crystal settling is  
712 probably the major process creating the anisotropy of the cumulates, rather than magma flow,  
713 crystal growth or compaction. Our data show that plastic deformation is present but not  
714 widely recorded in any minerals, even at the base of the section. We interpret this as

715 indicating a limited contribution of compaction or alternatively for an ongoing regional stress  
716 to the microstructure. From a purely microstructural aspect, this study emphasises the  
717 importance of crystal-shape control during the development of microstructures in cumulate  
718 rocks.

719

720 In the Trinity complex, magmatic processes gave rise to strong crystallographic preferred  
721 orientations for olivine, cpx and opx, similar to those classically attributed to plastic flow in  
722 the dislocation creep regime. Since these are likely to constrain the activation of favourably  
723 oriented slip systems during subsequent deformation, the reliability of their use as proxies for  
724 the conditions of deformation has to be regarded with caution.

725 Our results, along with those of previous structural and geochemical work, are consistent  
726 with (1) the mantle section of Trinity ophiolite representing a fossil marginal slow-spreading  
727 centre obducted onto the North American plate and (2) Bear Creek and similar intrusions  
728 corresponding to the late- to post-tectonic emplacement and differentiation of boninitic  
729 magmas in a subduction-related environment.

730 The microstructural data that we have presented may also have important implications for our  
731 understanding of the development of the fabrics in pyroxene-rich lithologies, which could be  
732 pre-conditioned by the initial magmatic fabric. The strong fabrics in the lithologies in the  
733 Bear Creek cumulates would also have important implications in terms of seismic anisotropy  
734 as they differ significantly from those of more classic mantle pyroxenites.

735

### 736 **Acknowledgments**

737 We are grateful to M. Bebbington and F. de Parseval for providing high-quality polished thin  
738 sections for EBSD measurements. We would also like to thank T. Murphy for his assistance  
739 during lab work and Patrick Launeau for stimulating discussions on magmatic processes. We

740 would like to thank Károly Hidas and four anonymous reviewers who greatly contributed in  
741 improving the quality and flow of the manuscript. This work was supported by the Australian  
742 Research Council grant for the ARC Centre of Excellence for Core to Crust Fluid Systems  
743 (CCFS), a Macquarie University International Postgraduate Scholarship (H.H.), Macquarie  
744 postgraduate funds (H.H.), and CNRS-INSU funds (UMR 5563, Géosciences Environnement  
745 Toulouse). The project used instrumentation funded by ARC LIEF and DEST Systemic  
746 Infrastructure Grants, Macquarie University, NCRIS AuScope and industry partners. This is  
747 contribution XXX from the ARC Centre of Excellence for Core to Crust Fluid System  
748 ([www.ccfs.mq.edu.au](http://www.ccfs.mq.edu.au)) and XXX from the GEMOC Key Centre ([www.gemoc.mq.edu.au](http://www.gemoc.mq.edu.au)).

749

750 Declarations of interest: none

751

## References

752  
753

- 754 Achenbach, K.L., Cheadle, M.J., Faul, U., Kelemen, P., Swapp, S., 2011. Lattice-preferred  
755 orientation and microstructure of peridotites from ODP Hole 1274A (15°39'N), Mid-Atlantic  
756 Ridge: Testing models of mantle upwelling and tectonic exhumation. *Earth and Planetary  
757 Science Letters* 301, 199-212.
- 758 Avé Lallemant, H.G., Carter, N.L., 1970. Syntectonic Recrystallization of Olivine and Modes of  
759 Flow in the Upper Mantle. *Geological Society of America Bulletin* 81, 2203-2220.
- 760 Bachmann, F., Hielscher, R., Jupp, P.E., Pantleon, W., Schaeben, H., Wegert, E., 2010a.  
761 Inferential statistics of electron backscatter diffraction data from within individual  
762 crystalline grains. *Journal of Applied Crystallography* 43, 1338-1355.
- 763 Bachmann, F., Hielscher, R., Schaeben, H., 2010b. Texture Analysis with MTEX – Free and  
764 Open Source Software Toolbox. *Solid State Phenomena* 160, 63-68.
- 765 Bachmann, F., Hielscher, R., Schaeben, H., 2011. Grain detection from 2d and 3d EBSD  
766 data—Specification of the MTEX algorithm. *Ultramicroscopy* 111, 1720-1733.
- 767 Bascou, J., Tommasi, A., Mainprice, D., 2002. Plastic deformation and development of  
768 clinopyroxene lattice preferred orientations in eclogites. *Journal of Structural Geology* 24,  
769 1357-1368.
- 770 Benn, K., Allard, B., 1989. Preferred Mineral Orientations Related to Magmatic Flow in  
771 Ophiolite Layered Gabbros. *Journal of Petrology* 30, 925-946.
- 772 Biedermann, A.R., Heidelbach, F., Jackson, M., Bilardello, D., McEnroe, S.A., 2016. Magnetic  
773 fabrics in the Bjerkreim Sokndal Layered Intrusion, Rogaland, southern Norway: Mineral  
774 sources and geological significance. *Tectonophysics* 688, 101-118.
- 775 Bodinier, J.-L., Godard, M., 2003. Orogenic, ophiolitic, and abyssal peridotites. *Treatise on  
776 geochemistry* 2, 568.
- 777 Boorman, S., Boudreau, A., Kruger, F.J., 2004. The Lower Zone–Critical Zone Transition of  
778 the Bushveld Complex: a Quantitative Textural Study. *Journal of Petrology* 45, 1209-1235.
- 779 Boudier, F., 1991. Olivine xenocrysts in picritic magmas. *Contrib Mineral Petrol* 109, 114-  
780 123.
- 781 Boudier, F., Le Sueur, E., Nicolas, A., 1989. Structure of an atypical ophiolite: The Trinity  
782 complex, eastern Klamath Mountains, California. *Geological Society of America Bulletin* 101,  
783 820-833.
- 784 Boudreau, A.E., McBirney, A.R., 1997. The Skaergaard Layered Series. Part III. Non-dynamic  
785 Layering. *Journal of Petrology* 38, 1003-1020.
- 786 Brothers, R., 1964. Petrofabric analyses of Rhum and Skaergaard layered rocks. *Journal of  
787 Petrology* 5, 255-274.
- 788 Brouxel, M., Lapierre, H., Michard, A., Albarède, F., 1988. Geochemical study of an early  
789 Paleozoic island-arc-back-arc basin system. Part 2: Eastern Klamath, early to middle  
790 Paleozoic island-arc volcanic rocks (northern California). *Geological Society of America  
791 Bulletin* 100, 1120-1130.
- 792 Bunge, H.J., 1982. *Texture analysis in materials science: mathematical methods*. Elsevier.
- 793 Cannat, M., Lécuyer, C., 1991. Ephemeral magma chambers in the Trinity peridotite,  
794 northern California. *Tectonophysics* 186, 313-328.
- 795 Cawthorn, R.G., Walraven, F., 1998. Emplacement and Crystallization Time for the Bushveld  
796 Complex. *Journal of Petrology* 39, 1669-1687.

797 Ceuleneer, G., Le Sueur, E., 2008. The Trinity ophiolite (California): the strange association of  
798 fertile mantle peridotite with ultra-depleted crustal cumulates. *Bulletin de la Societe*  
799 *Geologique de France* 179, 503-518.

800 Charlier, B., Namur, O., Latypov, R., Tegner, C., 2015. *Layered intrusions*, 1 ed.

801 Cheadle, M.J., Gee, J.S., 2017. Quantitative Textural Insights into the Formation of Gabbro in  
802 Mafic Intrusions. *Elements* 13, 409-414.

803 Clénet, H., Ceuleneer, G., Pinet, P., Abily, B., Daydou, Y., Harris, E., Amri, I., Dantas, C., 2010.  
804 Thick sections of layered ultramafic cumulates in the Oman ophiolite revealed by an  
805 airborne hyperspectral survey: Petrogenesis and relationship to mantle diapirism. *Lithos*  
806 114, 265-281.

807 Coleman, R.G., 1986. Ophiolites and accretion of the North American Cordillera. *Bulletin de*  
808 *la Societe Geologique de France* II, 961-968.

809 Dygert, N., Liang, Y., Kelemen, P.B., 2016. Formation of Plagioclase Lherzolite and Associated  
810 Dunite–Harzburgite–Lherzolite Sequences by Multiple Episodes of Melt Percolation and  
811 Melt–Rock Reaction: an Example from the Trinity Ophiolite, California, USA. *Journal of*  
812 *Petrology* 57, 815-838.

813 Feinberg, J.M., Wenk, H.-R., Scott, G.R., Renne, P.R., 2006. Preferred orientation and  
814 anisotropy of seismic and magnetic properties in gabbro-norites from the Bushveld layered  
815 intrusion. *Tectonophysics* 420, 345-356.

816 Frets, E., Tommasi, A., Garrido, C.J., Padrón-Navarta, J.A., Amri, I., Targuisti, K., 2012.  
817 Deformation processes and rheology of pyroxenites under lithospheric mantle conditions.  
818 *Journal of Structural Geology* 39, 138-157.

819 Helmstaedt, H., Anderson, O.L., Gavasci, A.T., 1972. Petrofabric studies of eclogite, spinel-  
820 Websterite, and spinel-lherzolite Xenoliths from kimberlite-bearing breccia pipes in  
821 southeastern Utah and northeastern Arizona. *Journal of Geophysical Research* 77, 4350-  
822 4365.

823 Henry, H., 2018. *Mantle Pyroxenites: Deformation and Seismic Properties*, Earth and  
824 *Planetary Department*. Macquarie University and Université Toulouse III.

825 Henry, H., Tilhac, R., Griffin, W.L., O'Reilly, S.Y., Satsukawa, T., Kaczmarek, M.-A., Grégoire,  
826 M., Ceuleneer, G., 2017. Deformation of mantle pyroxenites provides clues to geodynamic  
827 processes in subduction zones: Case study of the Cabo Ortegal Complex, Spain. *Earth and*  
828 *Planetary Science Letters* 472, 174-185.

829 Higgins, M.D., 1998. Origin of Anorthosite by Textural Coarsening: Quantitative  
830 Measurements of a Natural Sequence of Textural Development. *Journal of Petrology* 39,  
831 1307-1323.

832 Higgins, M.D., 2015. Quantitative Textural Analysis of Rocks in Layered Mafic Intrusions, in:  
833 Charlier, B., Namur, O., Latypov, R., Tegner, C. (Eds.), *Layered Intrusions*. Springer  
834 Netherlands, Dordrecht, pp. 153-181.

835 Holness, M.B., Sides, R., Prior, D.J., Cheadle, M.J., Upton, B.G., 2012. The peridotite plugs of  
836 Rum: Crystal settling and fabric development in magma conduits. *Lithos* 134, 23-40.

837 Holness, M.B., Vukmanovic, Z., Mariani, E., 2017. Assessing the role of compaction in the  
838 formation of adcumulates: a microstructural perspective. *Journal of Petrology* 58, 643-673.

839 Ismail, W.B., Mainprice, D., 1998. An olivine fabric database: an overview of upper mantle  
840 fabrics and seismic anisotropy. *Tectonophysics* 296, 145-157.

841 Jung, H., Karato, S.I., 2001. Water-Induced Fabric Transitions in Olivine. *Science* 293, 1460-  
842 1463.

843 Jung, H., Park, M., Jung, S., Lee, J., 2010. Lattice preferred orientation, water content, and  
844 seismic anisotropy of orthopyroxene. *J. Earth Sci.* 21, 555-568.

845 Kaczmarek, M.A., Bodinier, J.L., Bosch, D., Tommasi, A., Dautria, J.M., Kechid, S.A., 2016.  
846 Metasomatized Mantle Xenoliths as a Record of the Lithospheric Mantle Evolution of the  
847 Northern Edge of the Ahaggar Swell, In Teria (Algeria). *Journal of Petrology* 57, 345-382.

848 Karato, S.I., 2008. *Deformation of Earth Materials*. Cambridge.

849 Kelemen, P.B., Dick, H.J.B., Quick, J.E., 1992. Formation of harzburgite by pervasive  
850 melt/rock reaction in the upper mantle. *Nature* 358, 635-641.

851 Ko, B., Jung, H., 2015. Crystal preferred orientation of an amphibole experimentally  
852 deformed by simple shear. *Nature Communication* 6.

853 Kohlstedt, D.L., Holtzman, B.K., 2009. Shearing Melt Out of the Earth: An Experimentalist's  
854 Perspective on the Influence of Deformation on Melt Extraction. *Annual Review of Earth and  
855 Planetary Sciences* 37, 561-593.

856 Le Sueur, E., Boudier, F., Cannat, M., Ceuleneer, G., Nicolas, A., 1984. The Trinity mafic-  
857 ultramafic complex: first results of the structural study of an untypical ophiolite. *Ophioliti* 9,  
858 487-498.

859 Lindsley-Griffin, N., 1977. The Trinity ophiolite, Klamath Mountains, California. *Oregon  
860 Department of Geology and Mineral Industries Bulletin* 95, 107-120.

861 Mainprice, D., Bachmann, F., Hielscher, R., Schaeben, H., 2015. Descriptive tools for the  
862 analysis of texture projects with large datasets using MTEX: strength, symmetry and  
863 components. *Geological Society, London, Special Publications* 409, 251-271.

864 Mankinen, E.A., Lindsley-Griffin, N., Griffin, J.R., 2002. Concordant paleolatitudes for  
865 Neoproterozoic ophiolitic rocks of the Trinity Complex, Klamath Mountains, California.  
866 *Journal of Geophysical Research: Solid Earth* 107, EPM 11-11-EPM 11-18.

867 McBirney, A.R., Nicolas, A., 1997. The Skaergaard Layered Series. Part II. Magmatic flow and  
868 Dynamic Layering. *Journal of Petrology* 38, 569-580.

869 Michibayashi, K., Oohara, T., 2013. Olivine fabric evolution in a hydrated ductile shear zone  
870 at the Moho Transition Zone, Oman Ophiolite. *Earth and Planetary Science Letters* 377-378,  
871 299-310.

872 Moghadam, H.S., Li, Q., Griffin, W., Stern, R., Ishizuka, O., Henry, H., Lucci, F., O'Reilly, S.,  
873 Ghorbani, G., 2020. Repeated magmatic buildup and deep "hot zones" in continental  
874 evolution: The Cadomian crust of Iran. *Earth and Planetary Science Letters* 531, 115989.

875 Namur, O., Abily, B., Boudreau, A.E., Blanchette, F., Bush, J.W.M., Ceuleneer, G., Charlier, B.,  
876 Donaldson, C.H., Duchesne, J.-C., Higgins, M.D., Morata, D., Nielsen, T.F.D., O'Driscoll, B.,  
877 Pang, K.N., Peacock, T., Spandler, C.J., Toramaru, A., Veksler, I.V., 2015. Igneous Layering in  
878 Basaltic Magma Chambers, in: Charlier, B., Namur, O., Latypov, R., Tegner, C. (Eds.), *Layered  
879 Intrusions*. Springer Netherlands, Dordrecht, pp. 75-152.

880 Nicolas, A., 1992. Kinematics in magmatic rocks with special reference to gabbros. *Journal of  
881 Petrology* 33, 891-915.

882 Nicolas, A., Christensen, N.I., 1987. Formation of Anisotropy in Upper Mantle Peridotites - A  
883 Review. Composition, structure and dynamics of the lithosphere-asthenosphere system,  
884 111-123.

885 O'Reilly, S.Y., Griffin, W.L., 2013. Moho vs crust-mantle boundary: Evolution of an idea.  
886 *Tectonophysics* 609, 535-546.

887 Paterson, M.S., 2001. A granular flow theory for the deformation of partially molten rock.  
888 *Tectonophysics* 335, 51-61.

889 Prior, D.J., Boyle, A.P., Brenker, F., Cheadle, M.C., Day, A., Lopez, G., Peruzzi, L., Potts, G.,  
890 Reddy, S., Spiess, R., Timms, N.E., Trimby, P., Wheeler, J., Zetterstrom, L., 1999. The  
891 application of electron backscatter diffraction and orientation contrast imaging in the SEM  
892 to textural problems in rocks. *American Mineralogist* 84, 1741-1759.

893 Qi, C., Hansen, L.N., Wallis, D., Holtzman, B.K., Kohlstedt, D.L., 2018. Crystallographic  
894 Preferred Orientation of Olivine in Sheared Partially Molten Rocks: The Source of the “a-c  
895 Switch”. *Geochemistry, Geophysics, Geosystems*.

896 Quick, J.E., 1981. Petrology and petrogenesis of the Trinity peridotite, An upper mantle  
897 diapir in the eastern Klamath Mountains, northern California. *Journal of Geophysical  
898 Research: Solid Earth* 86, 11837-11863.

899 Quick, J.E., 1982. The origin and significance of large, tabular dunite bodies in the Trinity  
900 peridotite, northern California. *Contrib Mineral Petrol* 78, 413-422.

901 Satsukawa, T., Ildefonse, B., Mainprice, D., Morales, L.F.G., Michibayashi, K., Barou, F., 2013.  
902 A database of plagioclase crystal preferred orientations (CPO) and microstructures &ndash;  
903 implications for CPO origin, strength, symmetry and seismic anisotropy in gabbroic rocks.  
904 *Solid Earth* 4, 511-542.

905 Skemer, P., Katayama, I., Jiang, Z., Karato, S.-i., 2005. The misorientation index:  
906 Development of a new method for calculating the strength of lattice-preferred orientation.  
907 *Tectonophysics* 411, 157-167.

908 Ulrich, S., Mainprice, D., 2005. Does cation ordering in omphacite influence development of  
909 lattice-preferred orientation? *Journal of Structural Geology* 27, 419-431.

910 Vukmanovic, Z., Holness, M., Monks, K., Andersen, J.Ø., 2018. The Skaergaard trough  
911 layering: sedimentation in a convecting magma chamber. *Contrib Mineral Petrol* 173, 43.

912 Wallin, E.T., Coleman, D.S., Lindsley-Griffin, N., Potter, A.W., 1995. Silurian plutonism in the  
913 Trinity terrane (Neoproterozoic and Ordovician), Klamath Mountains, California, United  
914 States. *Tectonics* 14, 1007-1013.

915 Wallin, E.T., Mattinson, J.M., Potter, A.W., 1988. Early Paleozoic magmatic events in the  
916 eastern Klamath Mountains, northern California. *Geology* 16, 144-148.

917 Wallin, E.T., Metcalf, Rodney V., 1998. Supra-Subduction Zone Ophiolite Formed in an  
918 Extensional Forearc: Trinity Terrane, Klamath Mountains, California. *The Journal of Geology*  
919 106, 591-608.

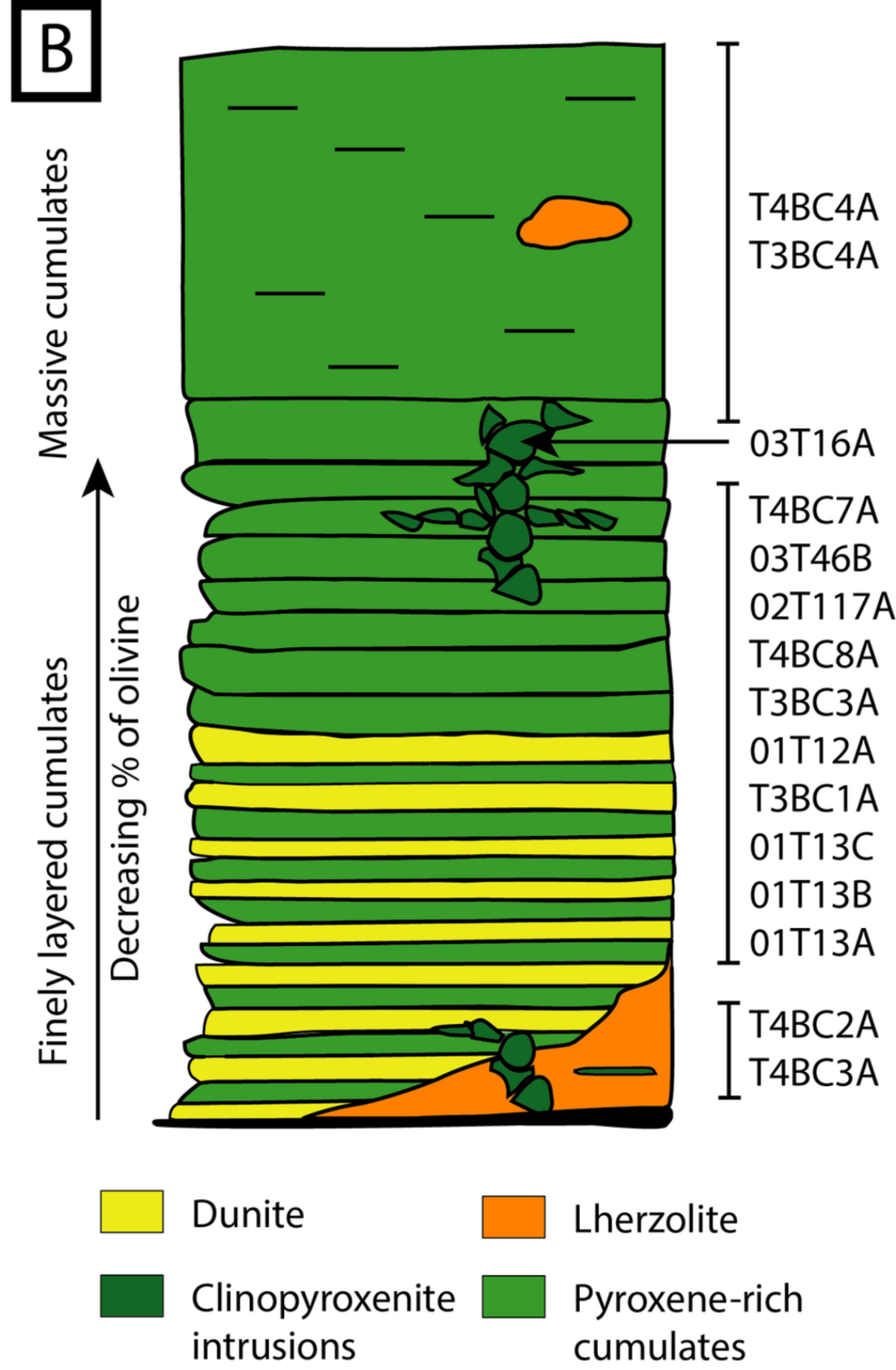
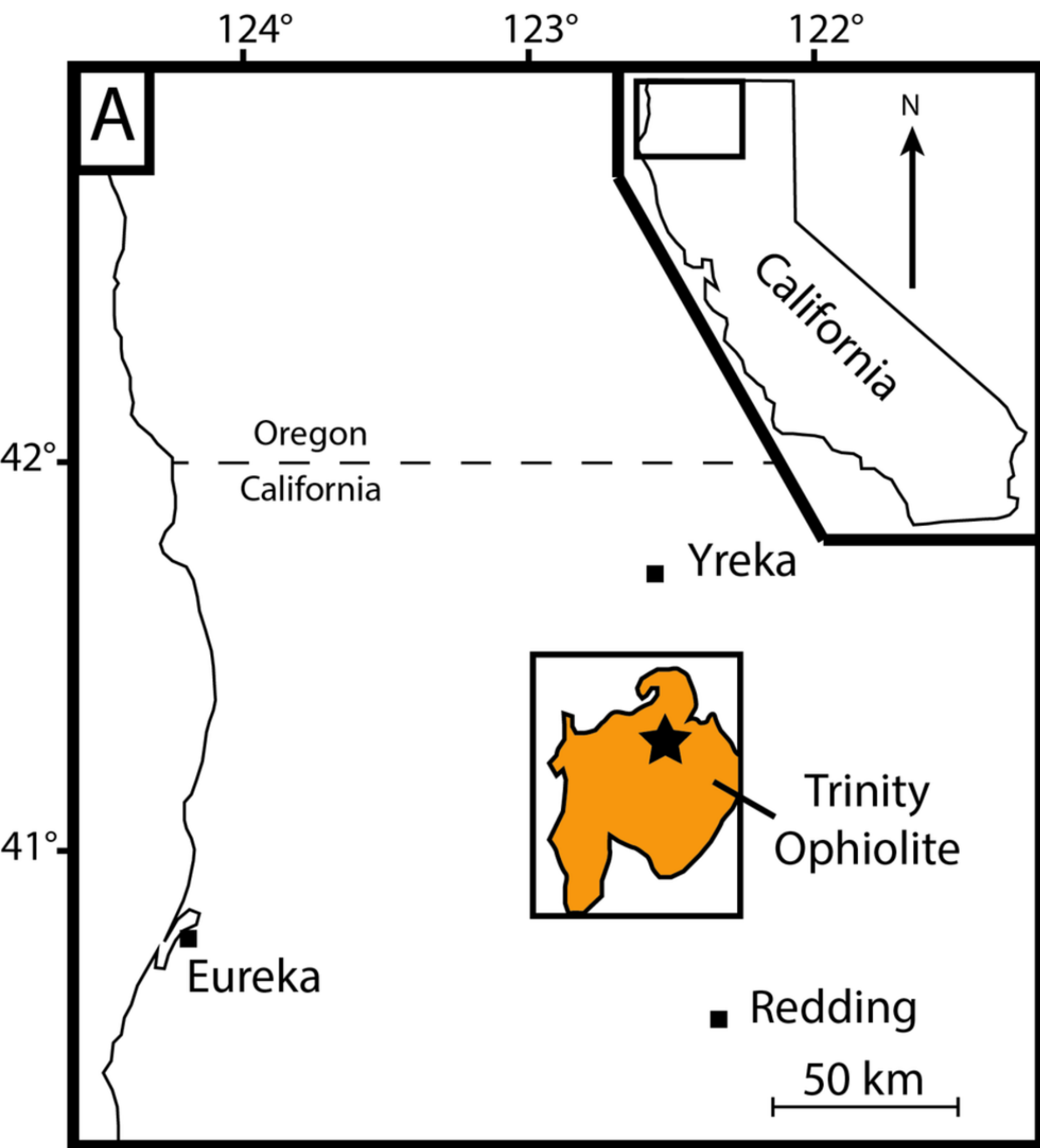
920 Williams, E., Boudreau, A.E., Boorman, S., Kruger, F.J., 2006. Textures of orthopyroxenites  
921 from the Burgersfort bulge of the eastern Bushveld Complex, Republic of South Africa.  
922 *Contrib Mineral Petrol* 151, 480-492.

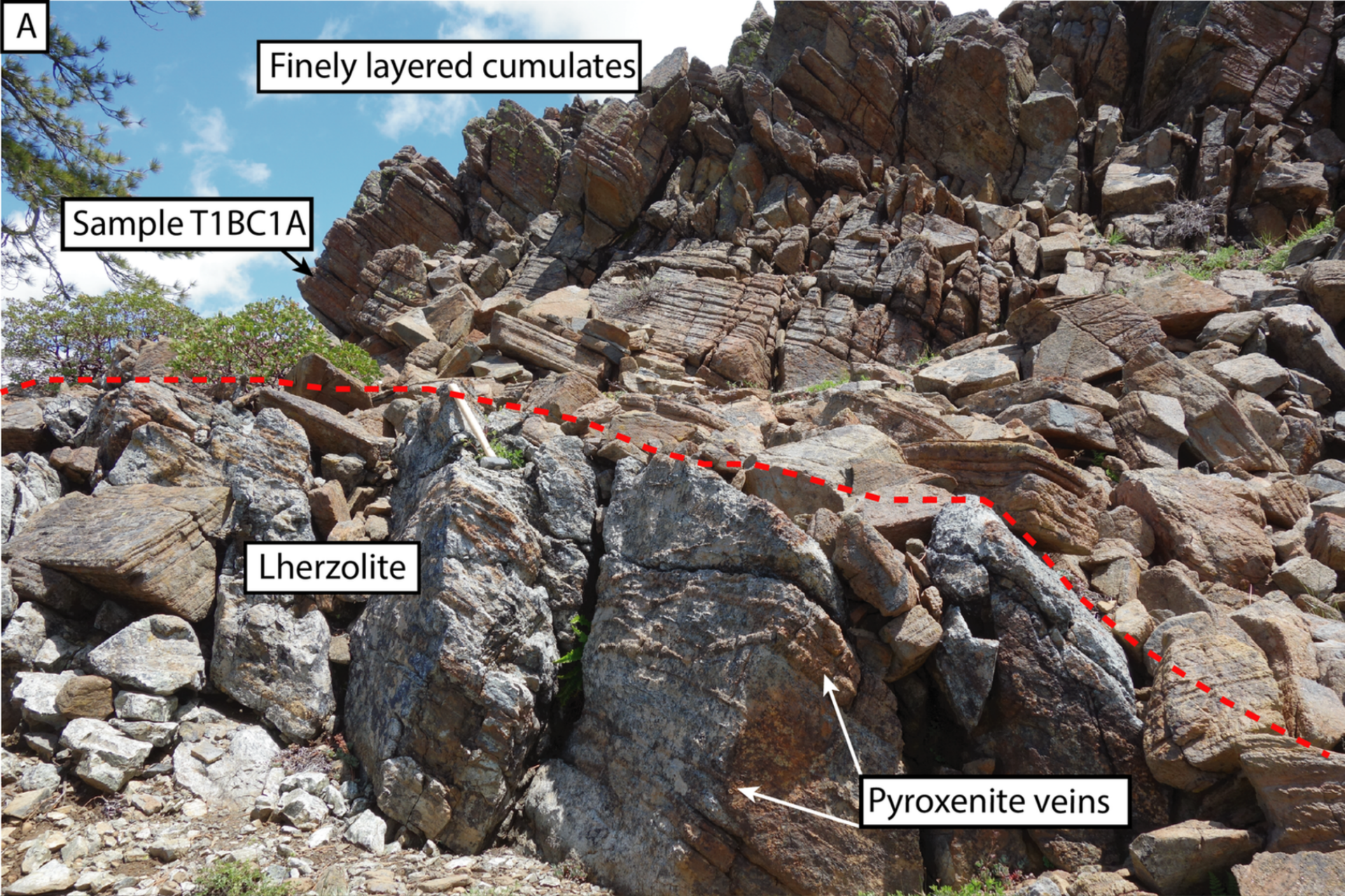
923 Wright, S.I., Nowell, M.M., Field, D.P., 2011. A Review of Strain Analysis Using Electron  
924 Backscatter Diffraction. *Microscopy and Microanalysis* 17, 316-329.

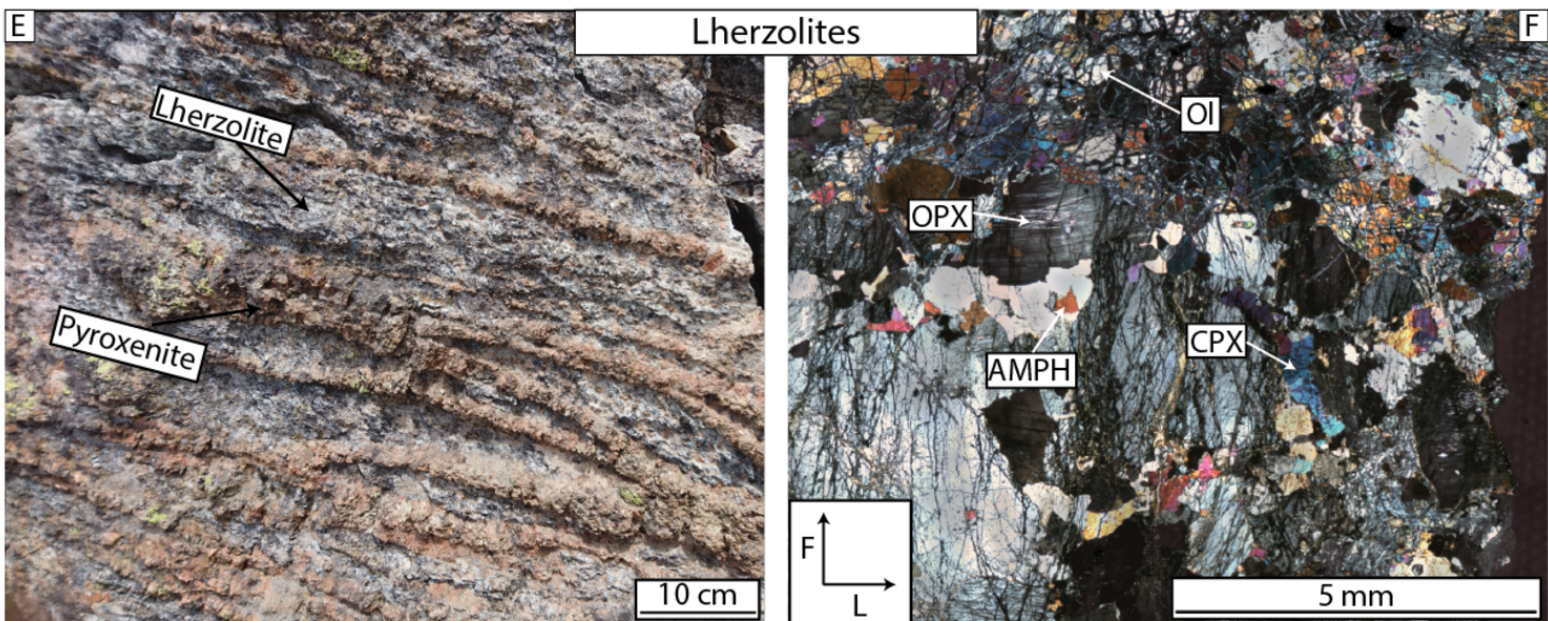
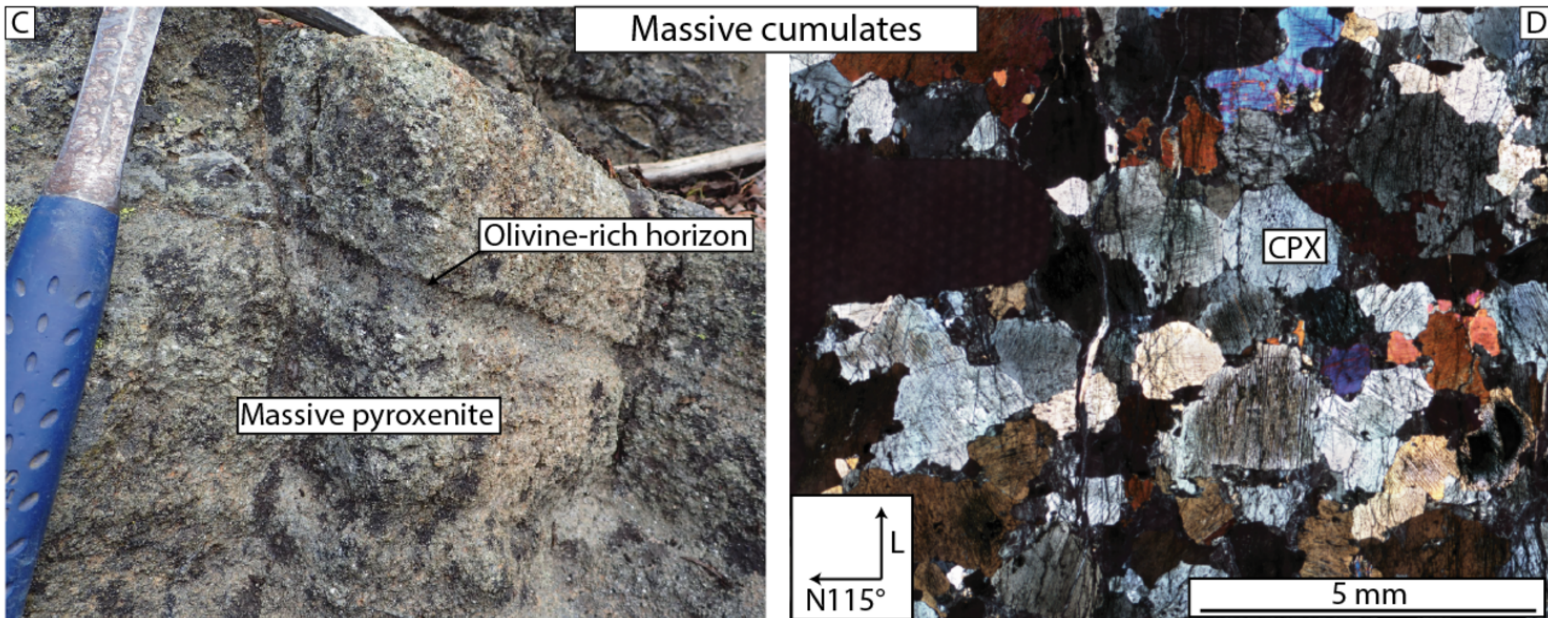
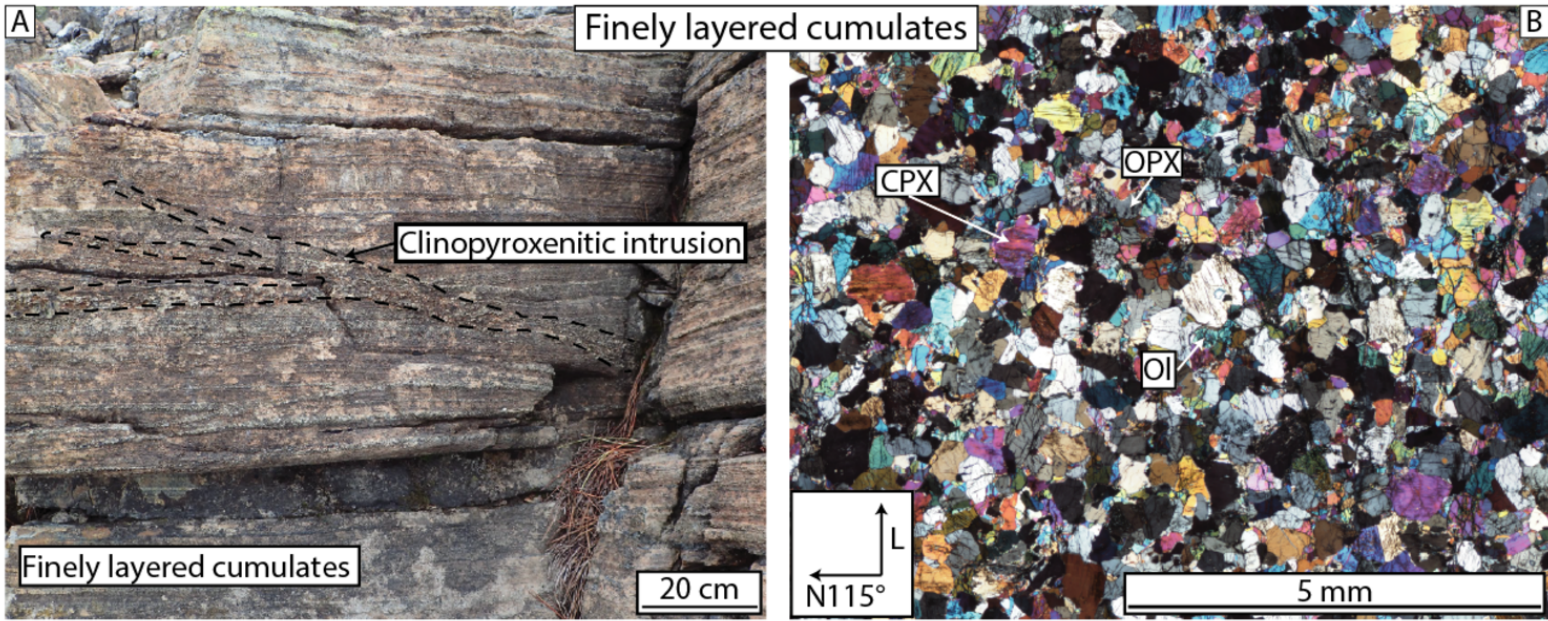
925 Yao, Z., Qin, K., Wang, Q., Xue, S., 2019. Weak B-type olivine fabric induced by fast  
926 compaction of crystal mush in a crustal magma reservoir. *Journal of Geophysical Research:  
927 Solid Earth* 0.

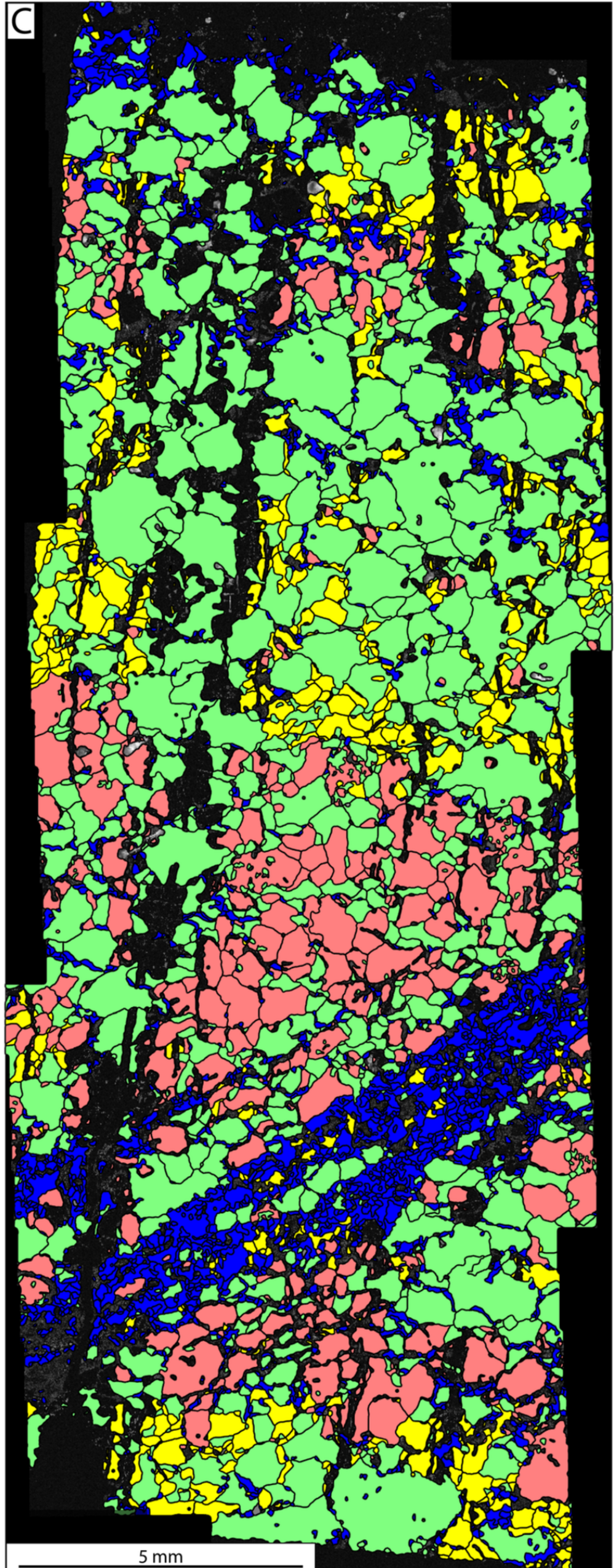
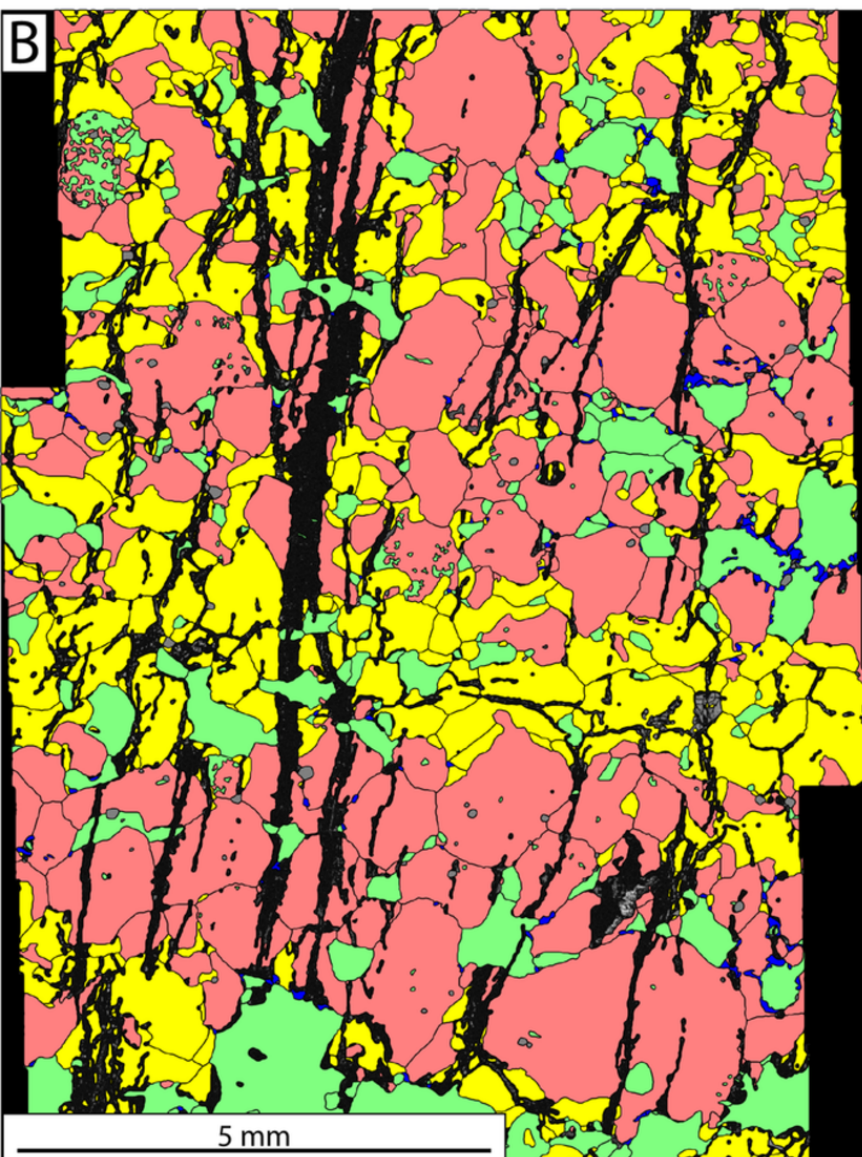
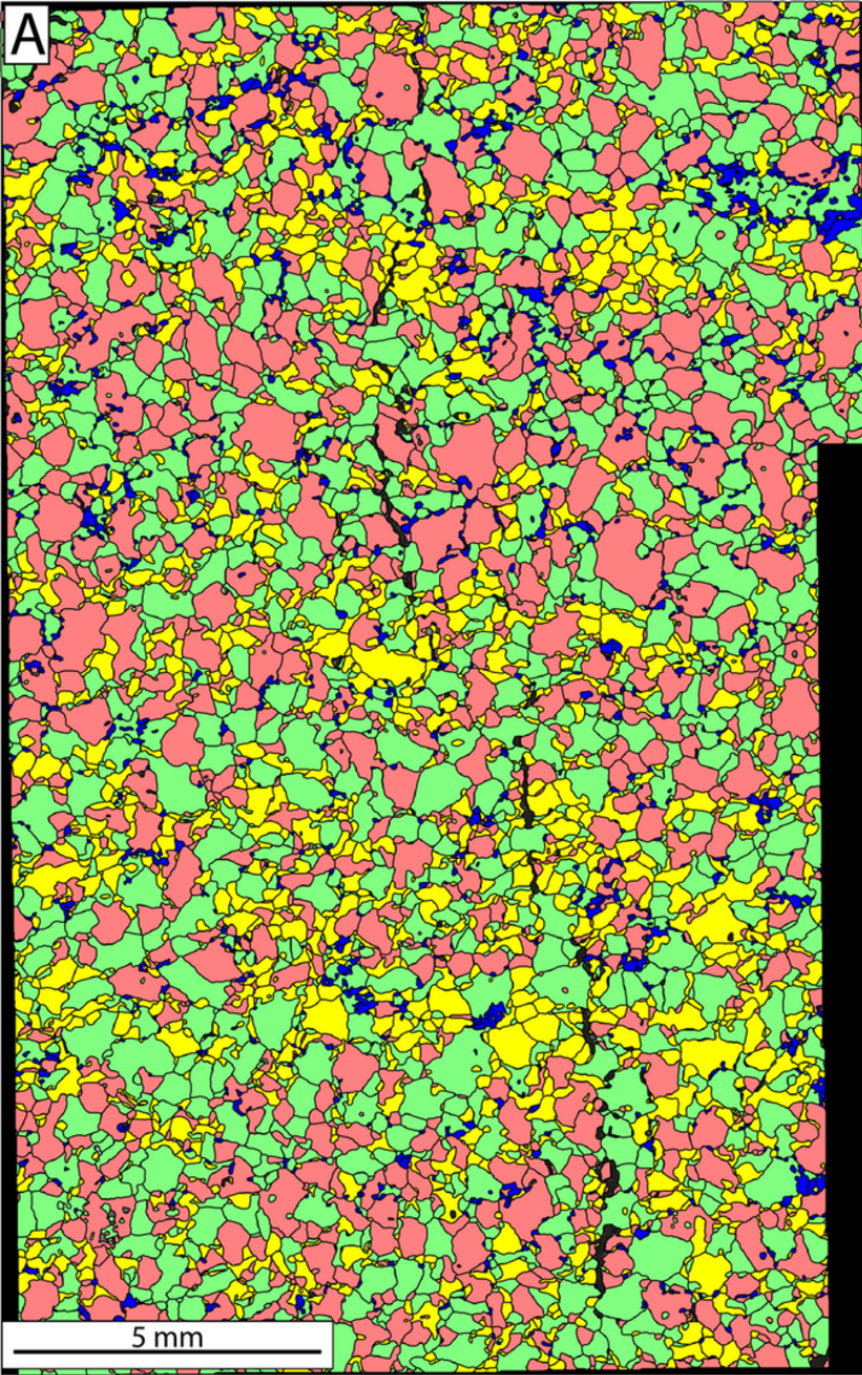
928 Ying, J., Zhang, H., Tang, Y., Su, B., Zhou, X., 2013. Diverse crustal components in pyroxenite  
929 xenoliths from Junan, Sulu orogenic belt: Implications for lithospheric modification invoked  
930 by continental subduction. *Chemical Geology* 356, 181-192.

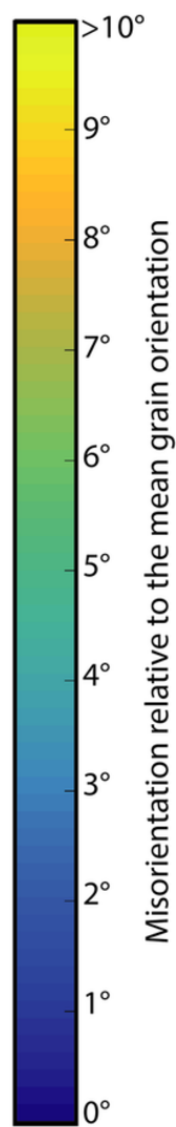
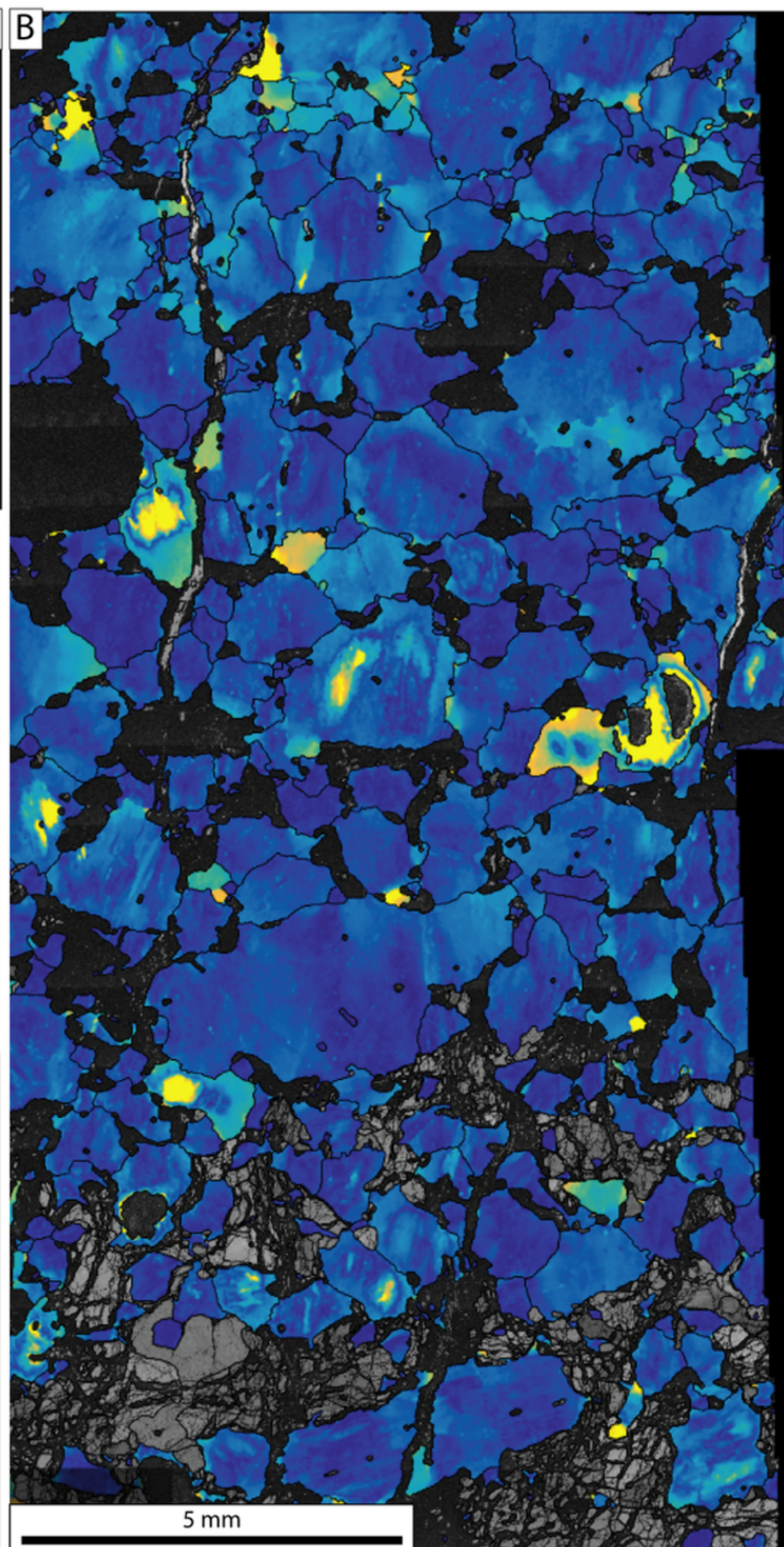
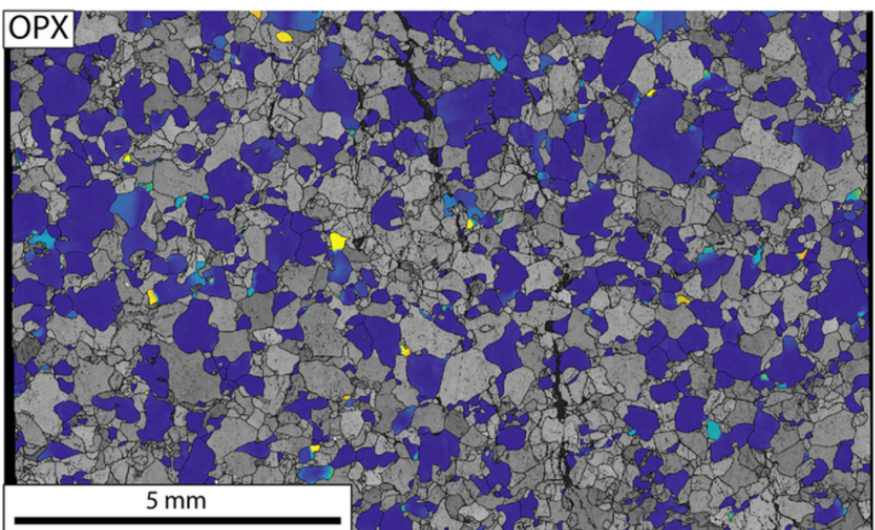
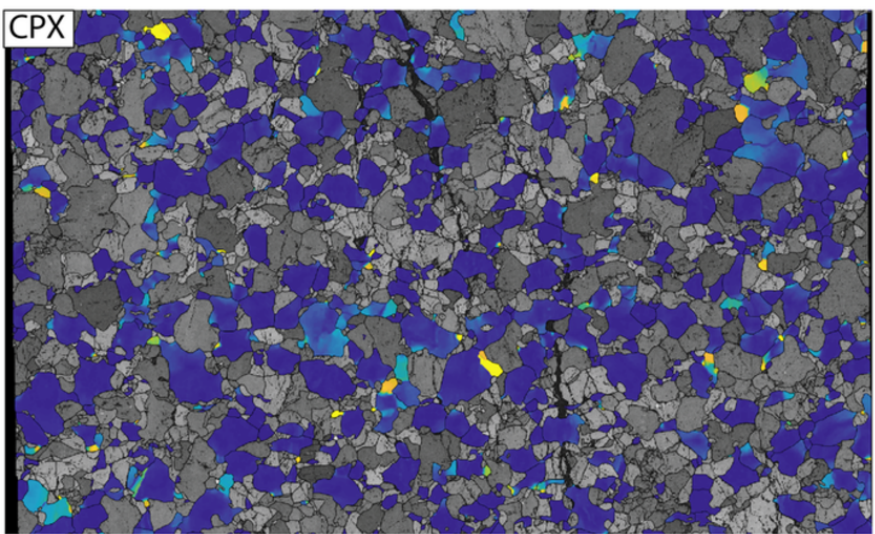
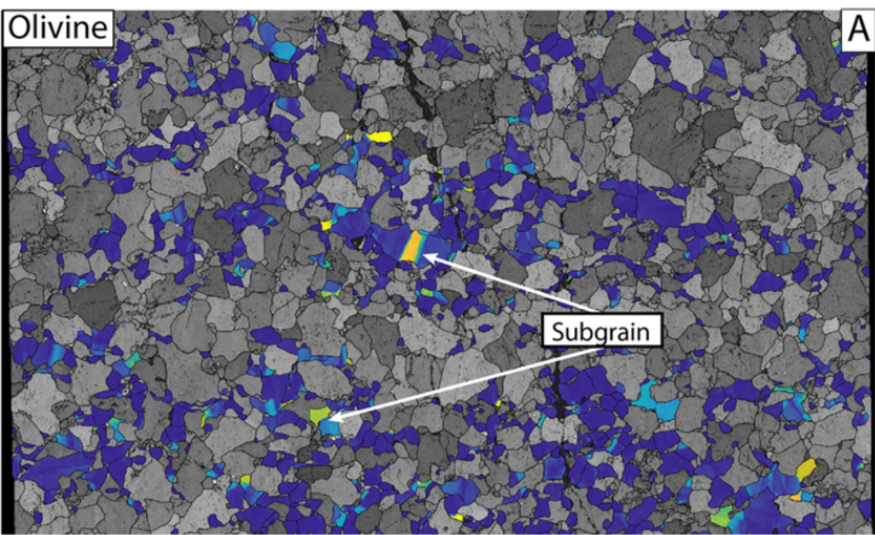
931



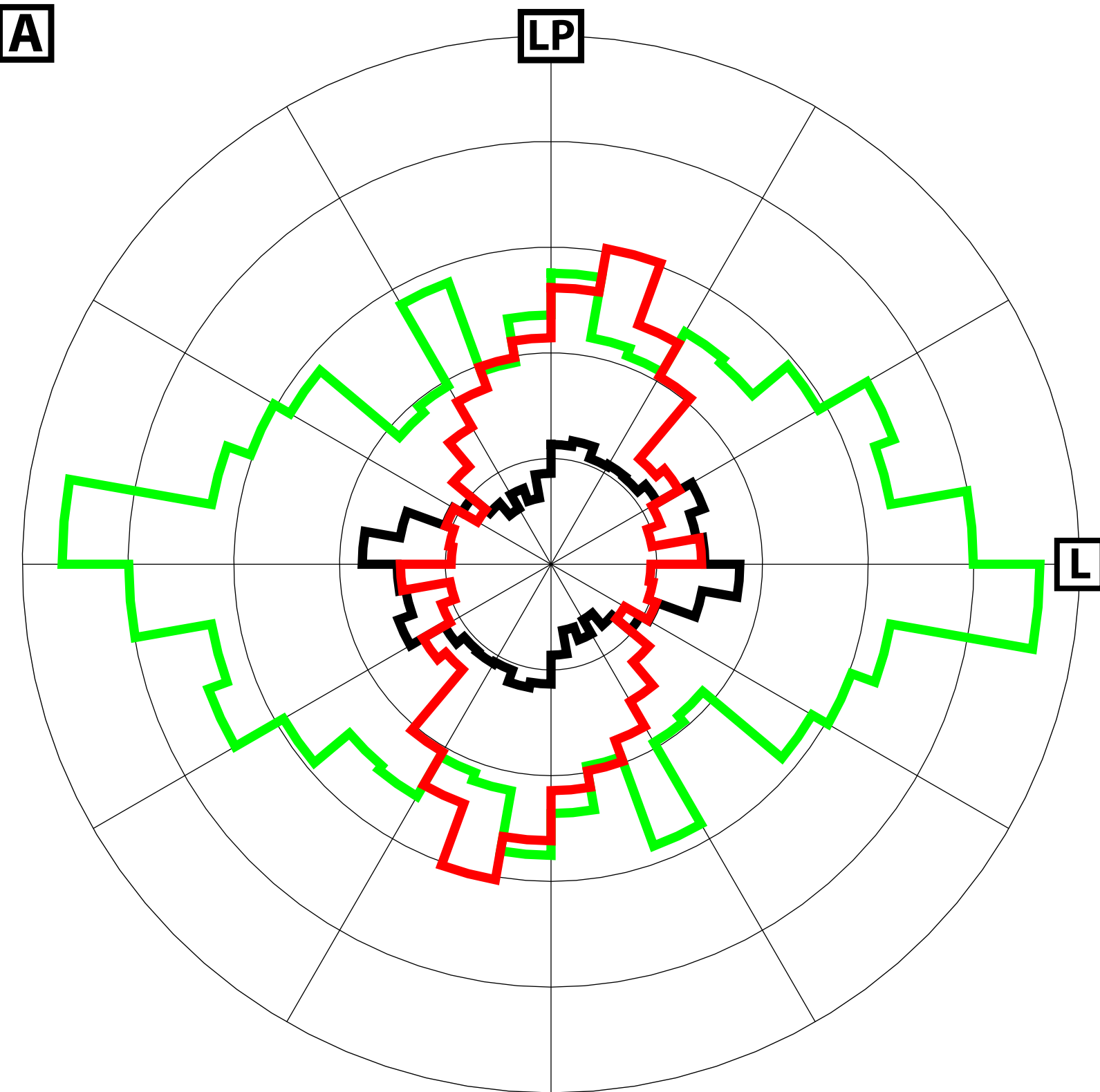




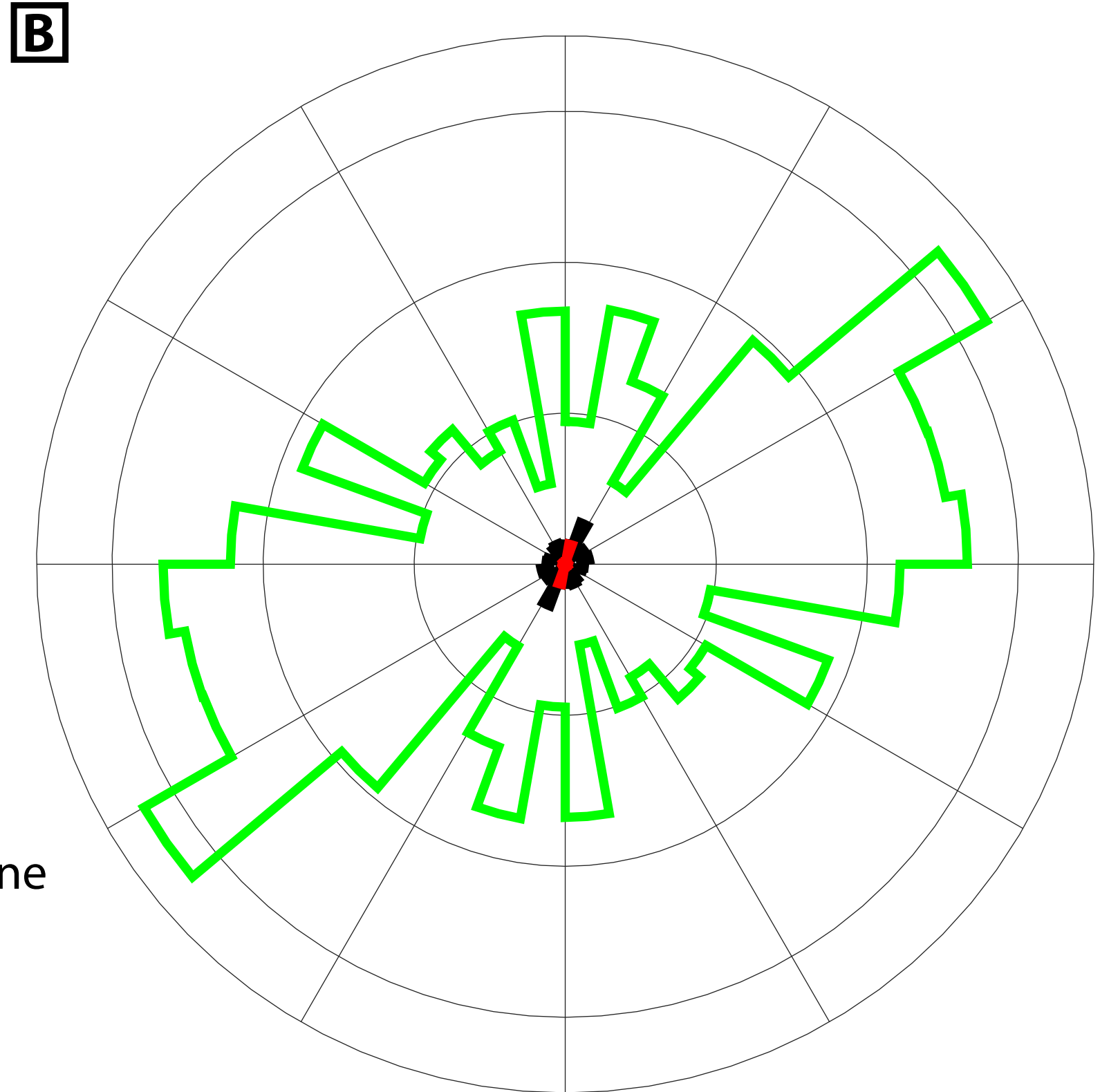




# Azimuth of olivine, cpx and opx grains' long axis in the Bear creek cumulates

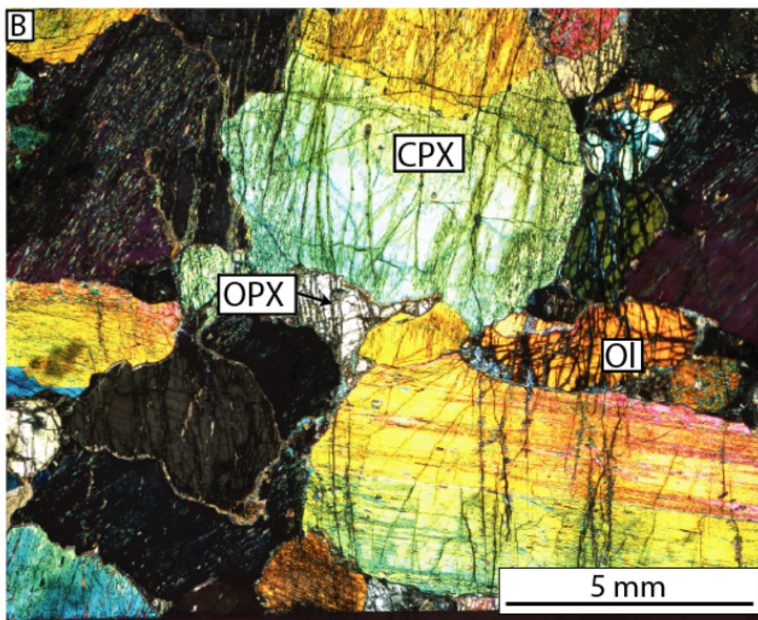
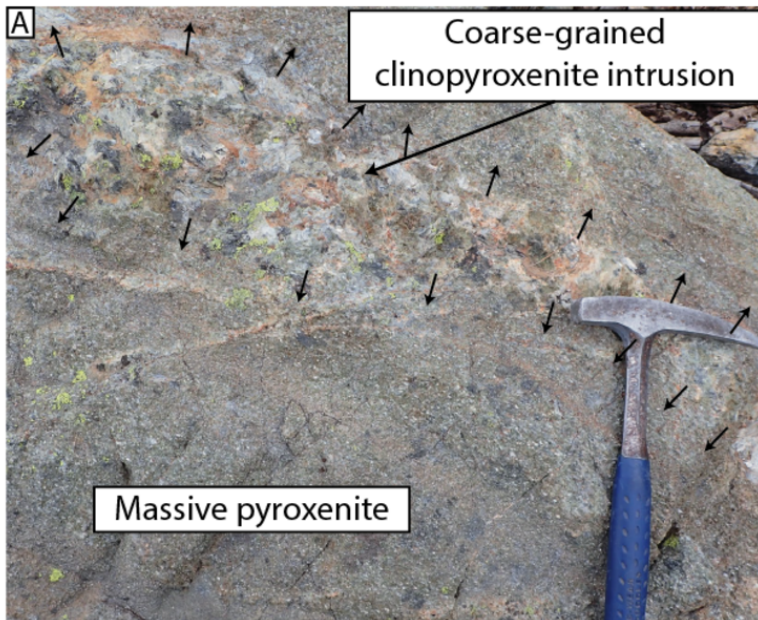


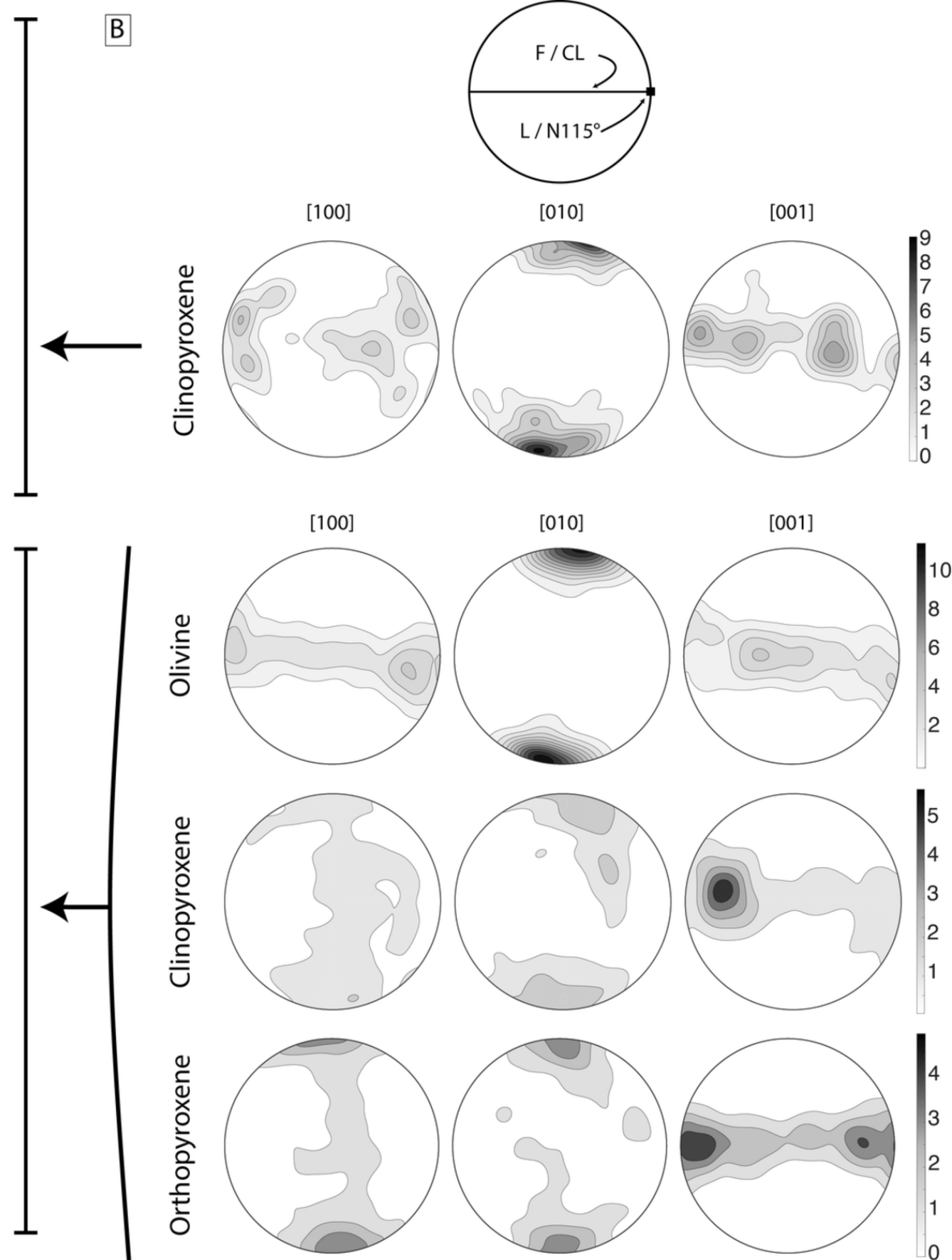
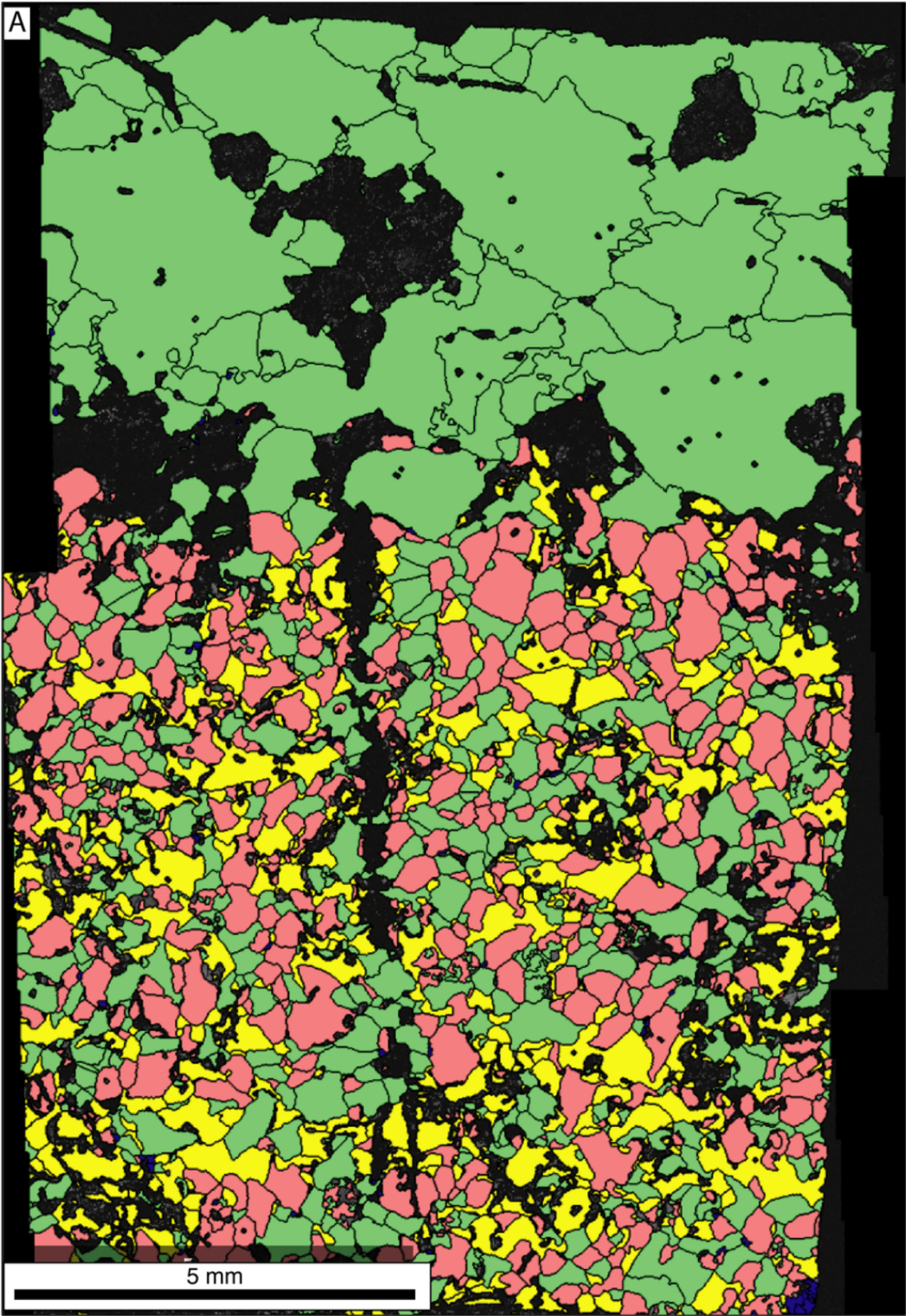
Finely layered cumulates



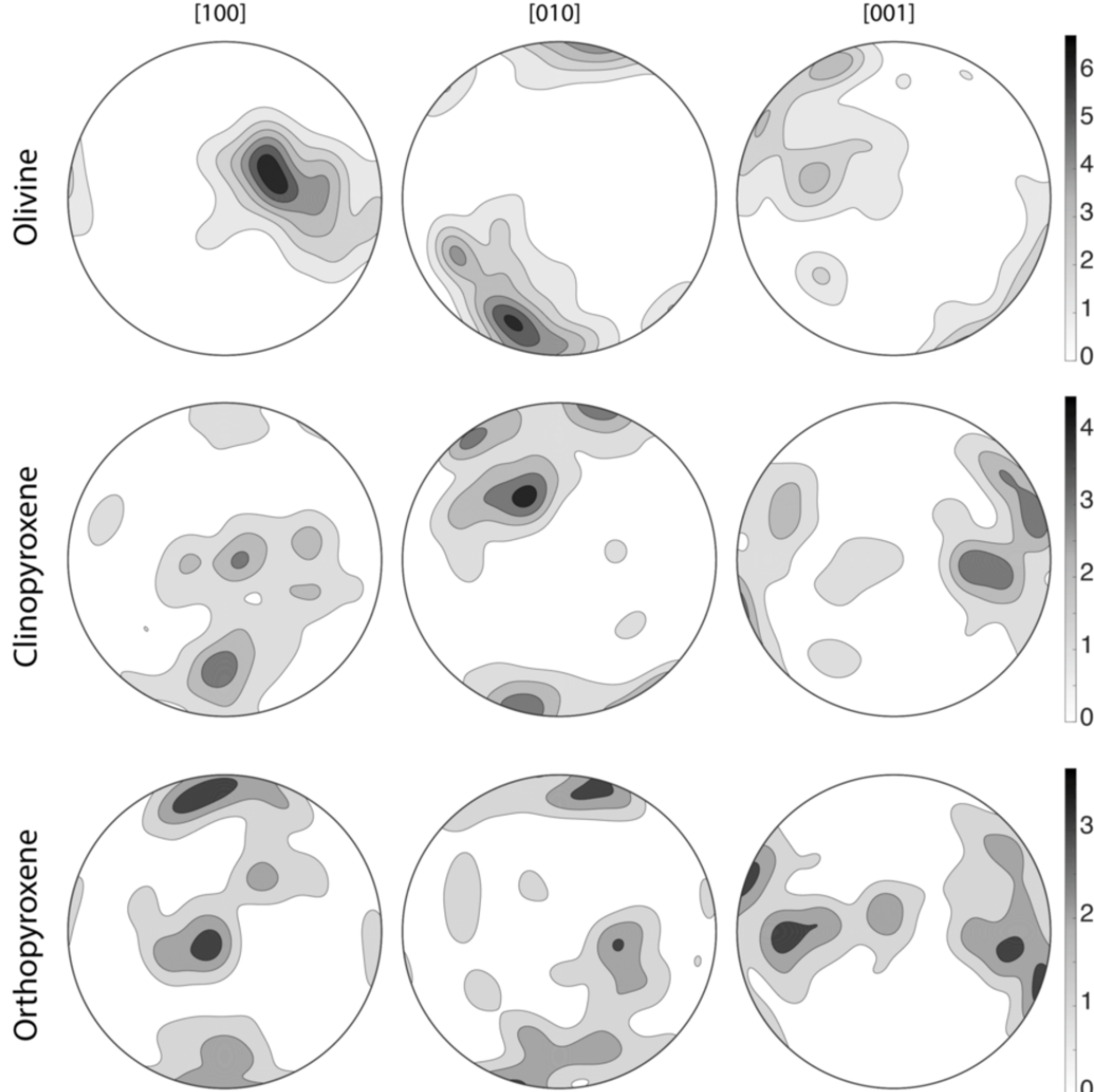
Massive cumulates

- Olivine
- Cpx
- Opx

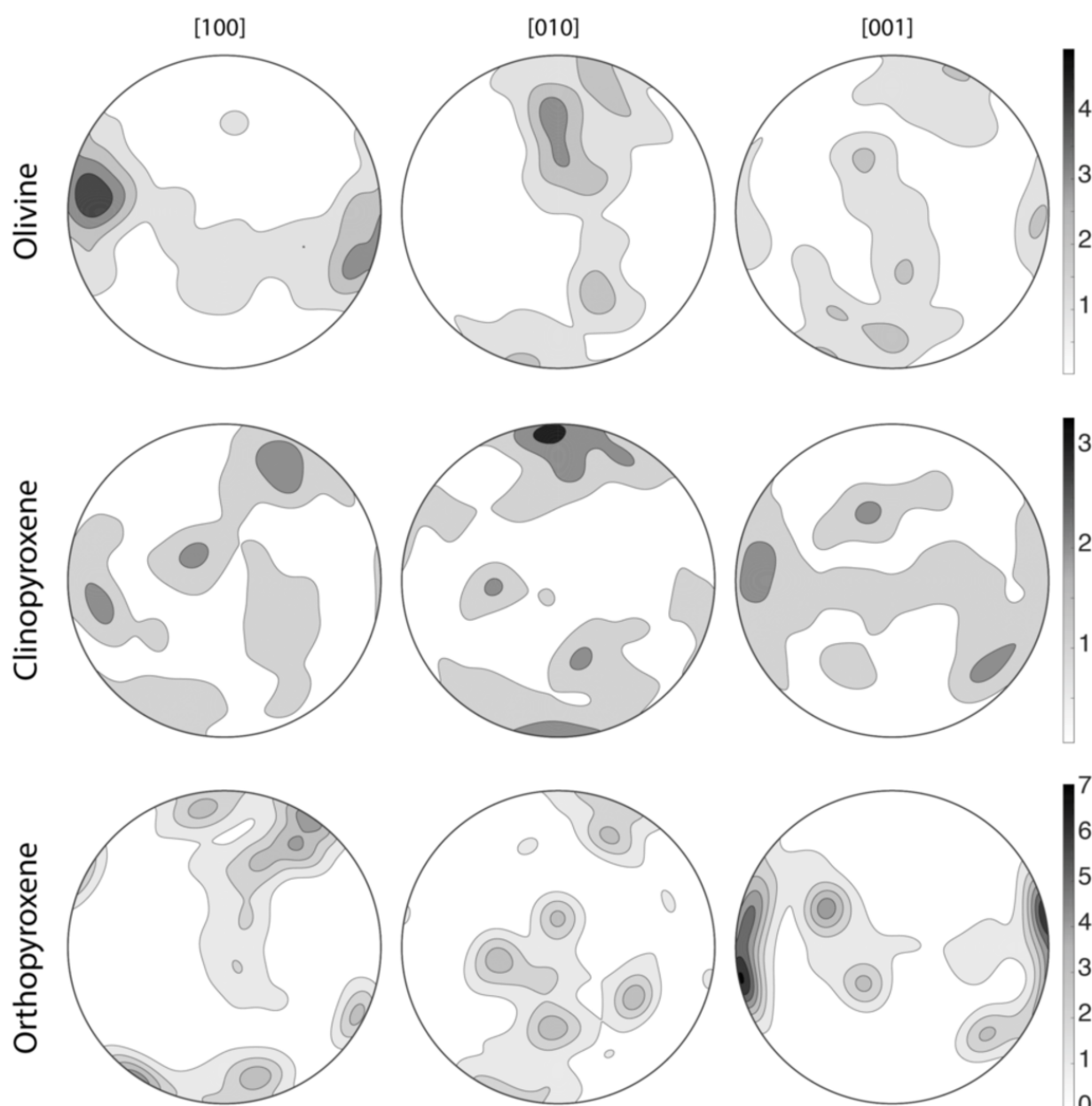


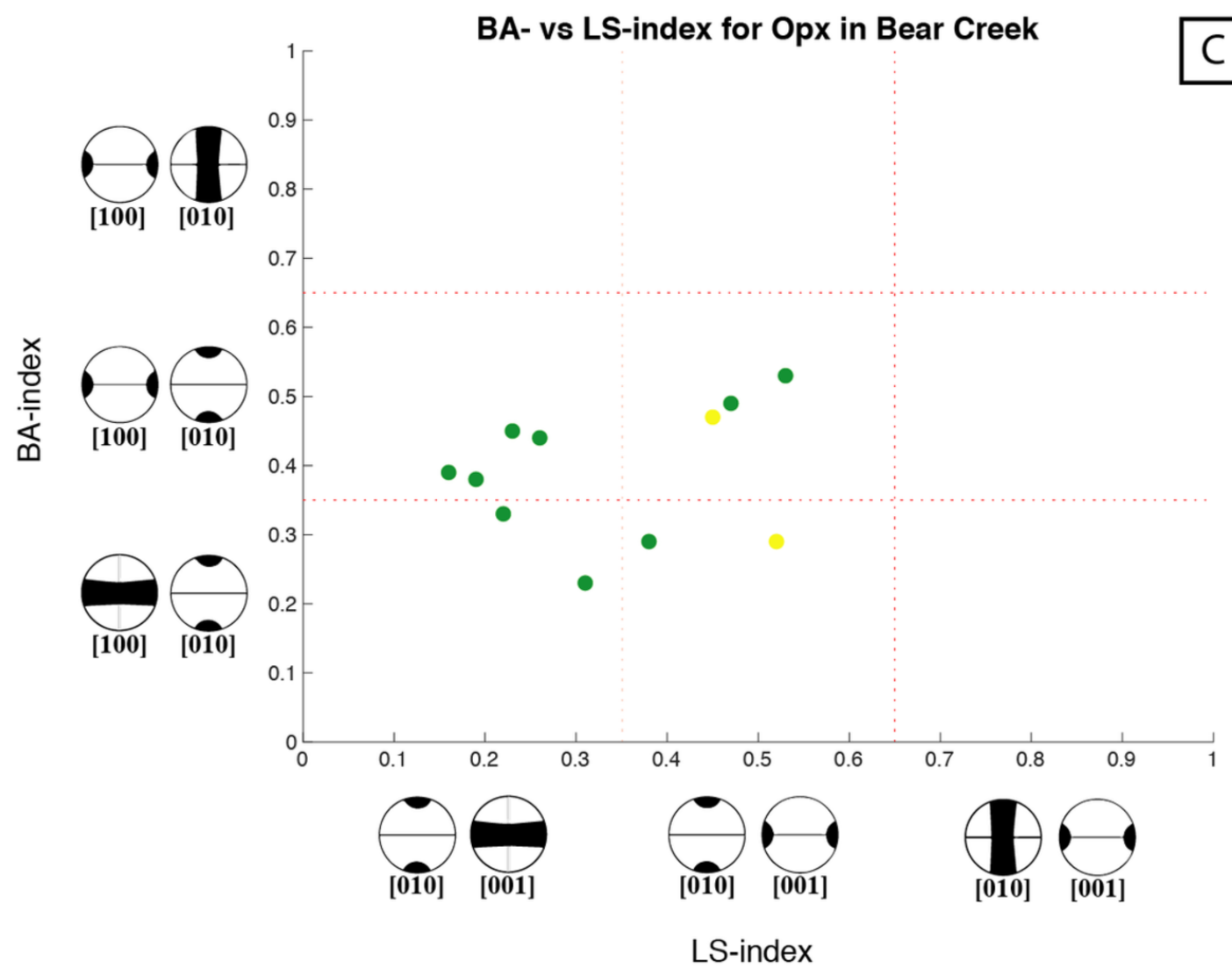
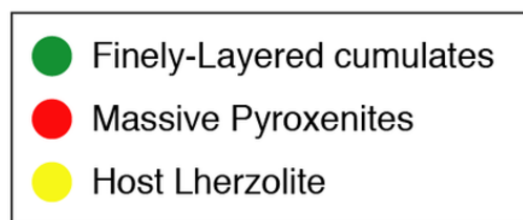
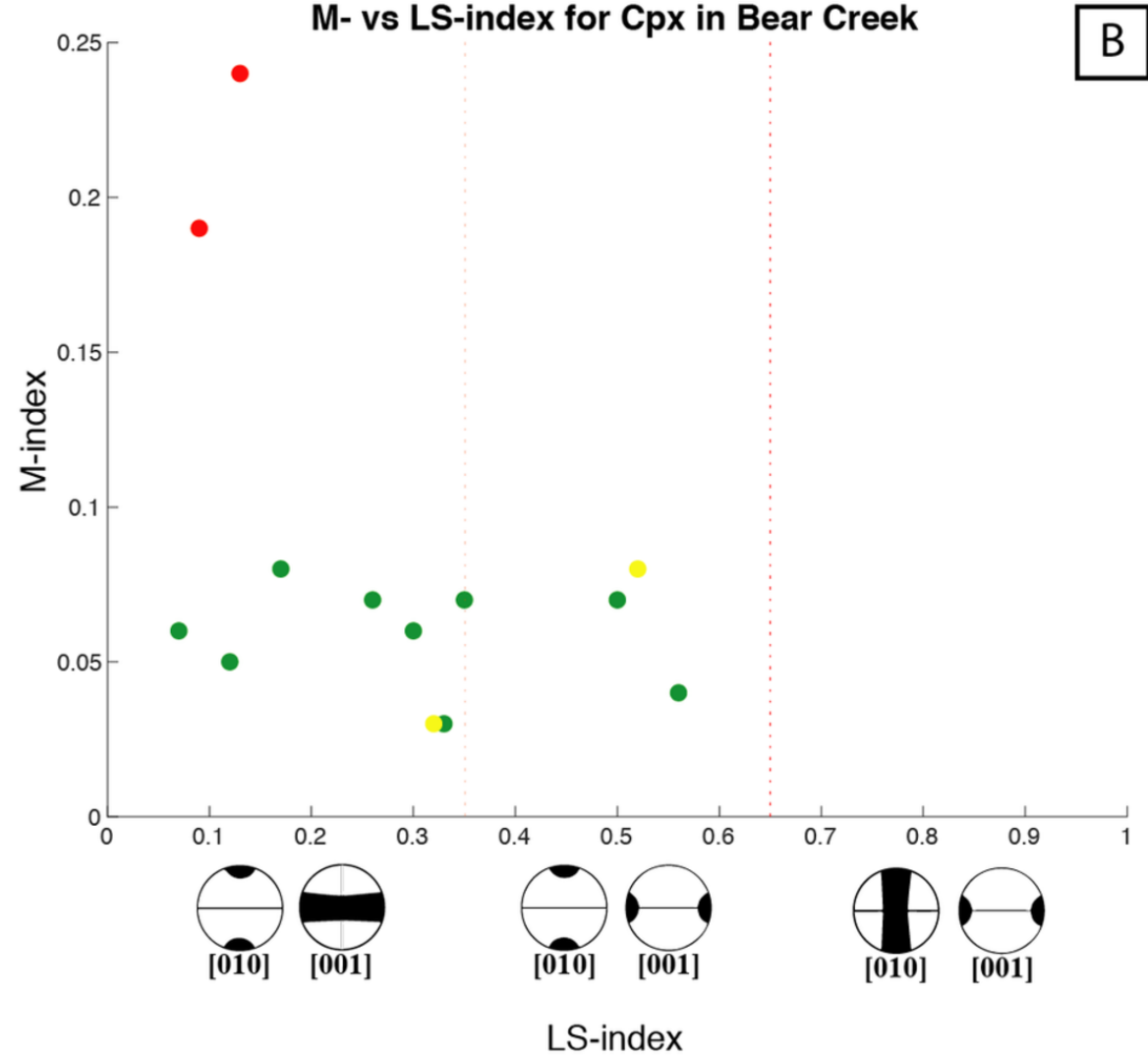
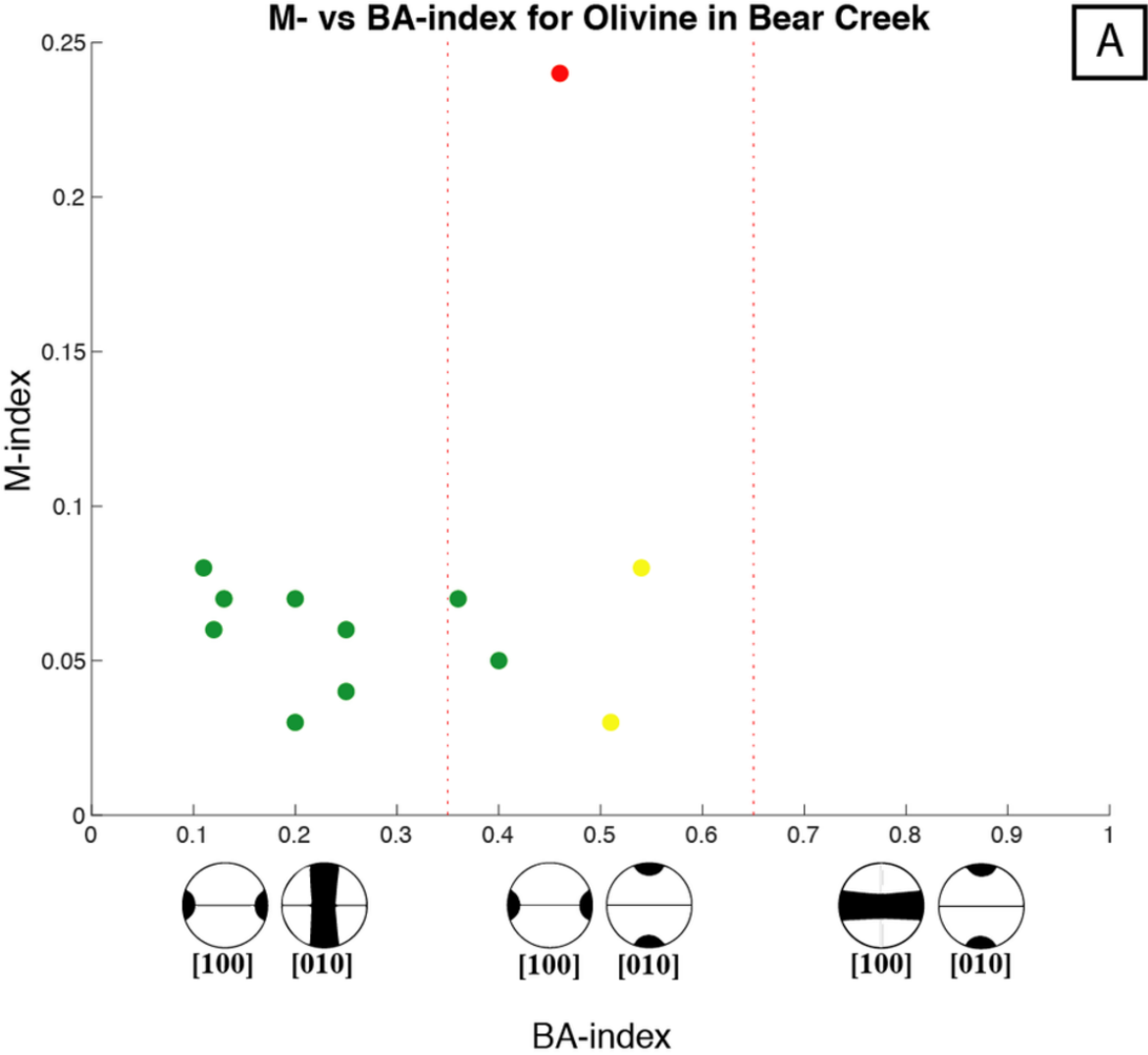


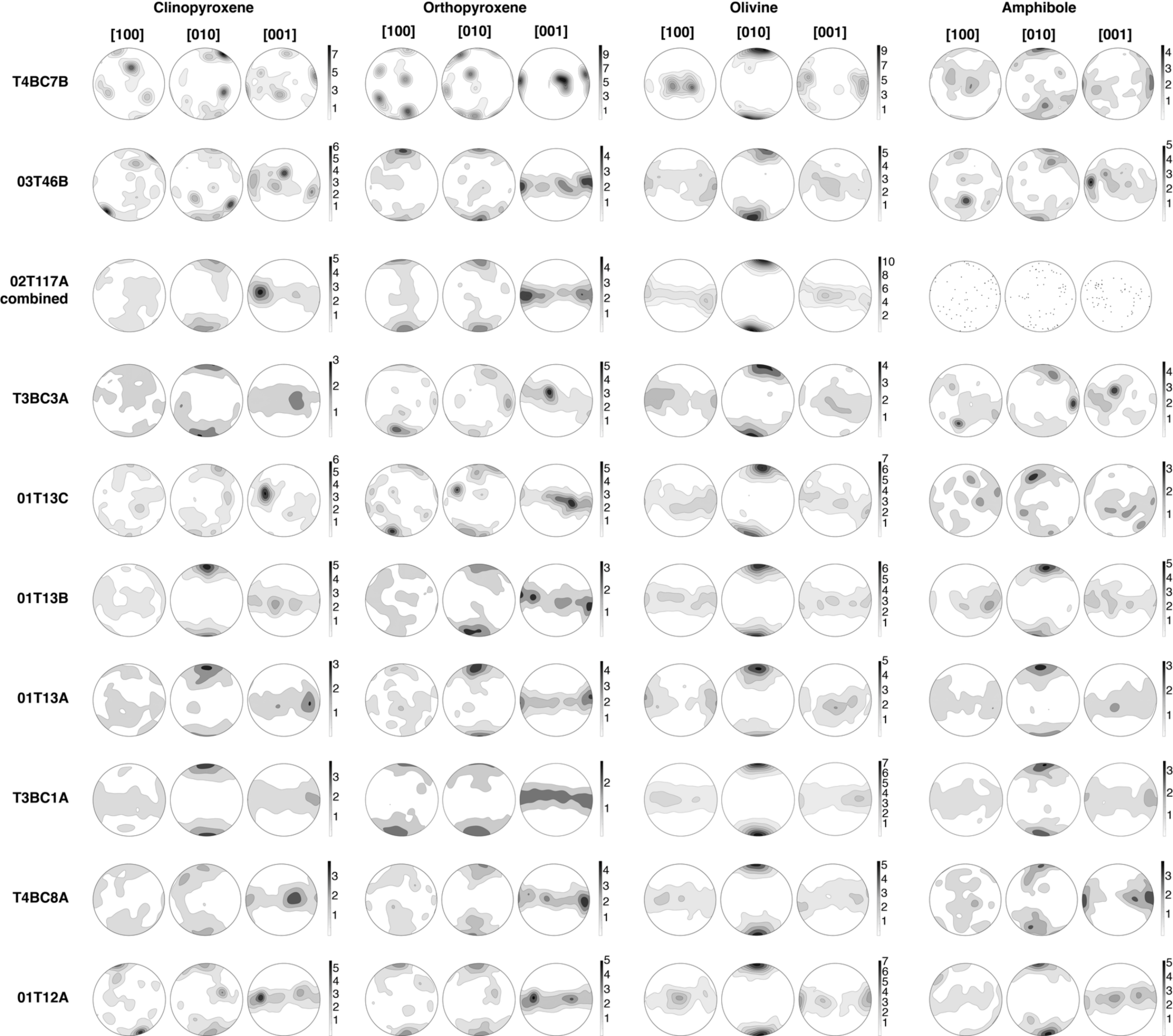
T4BC3



T4BC2

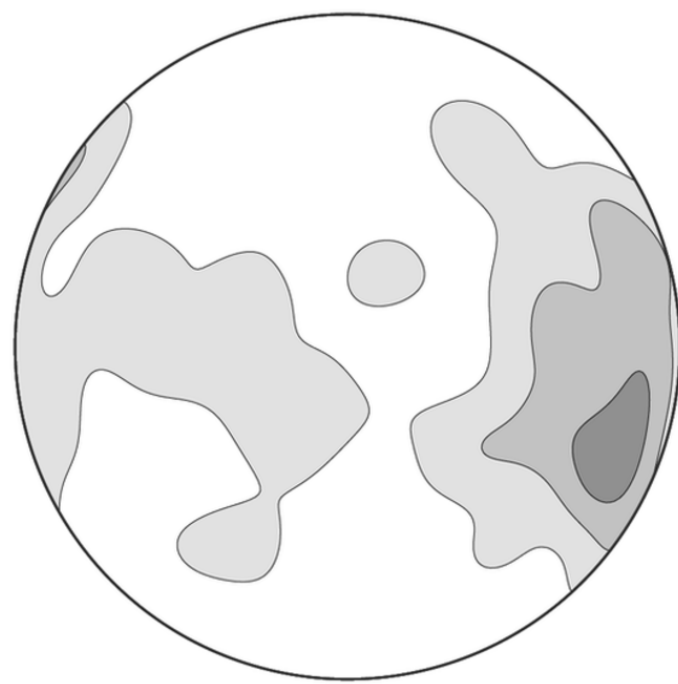
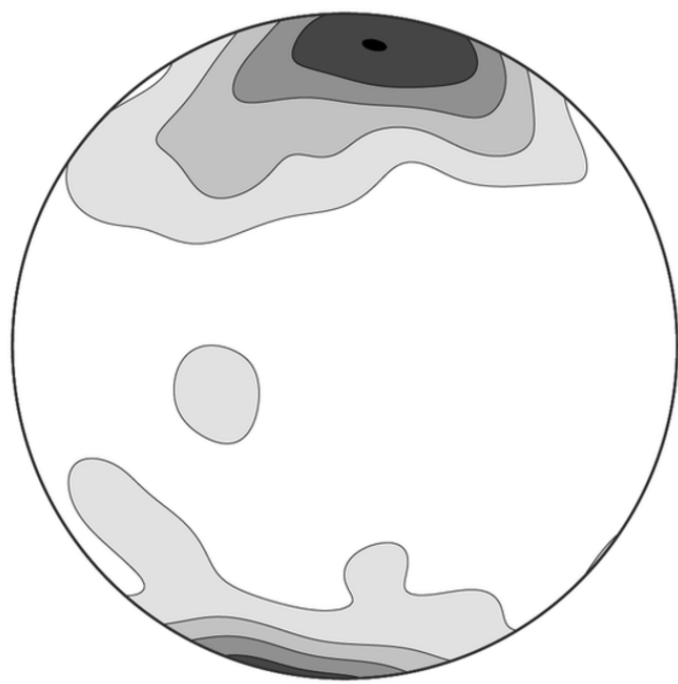
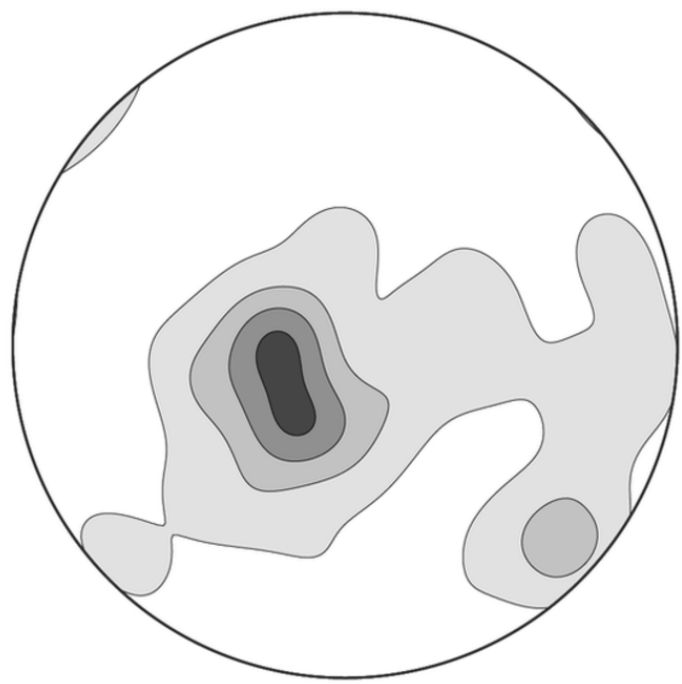




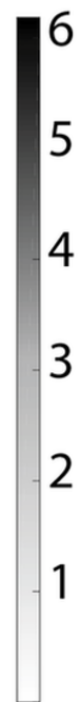
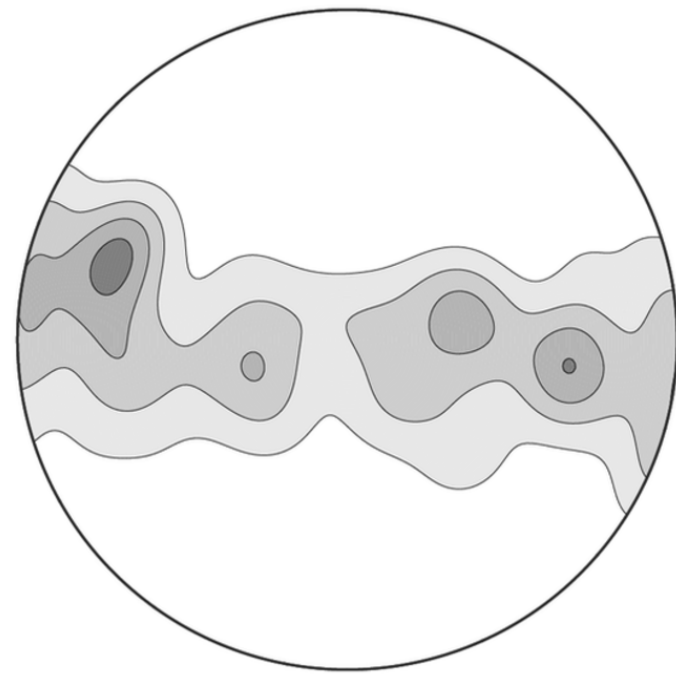
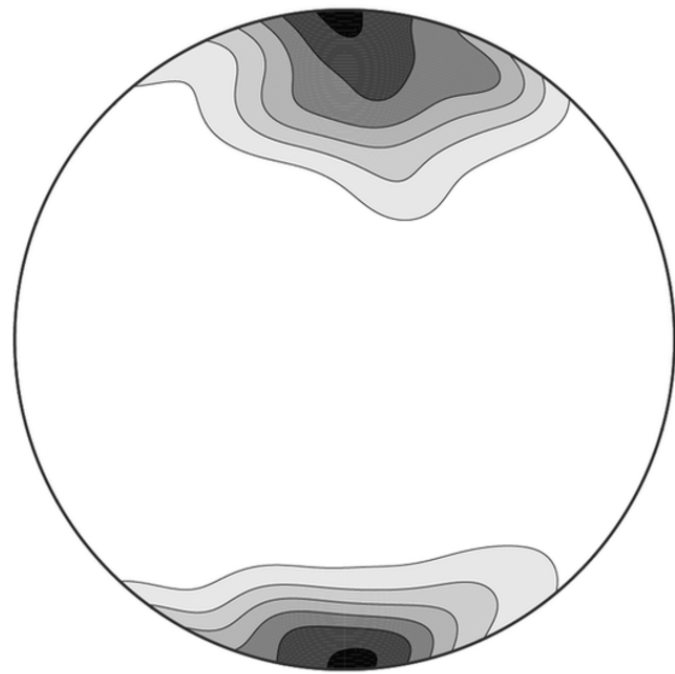
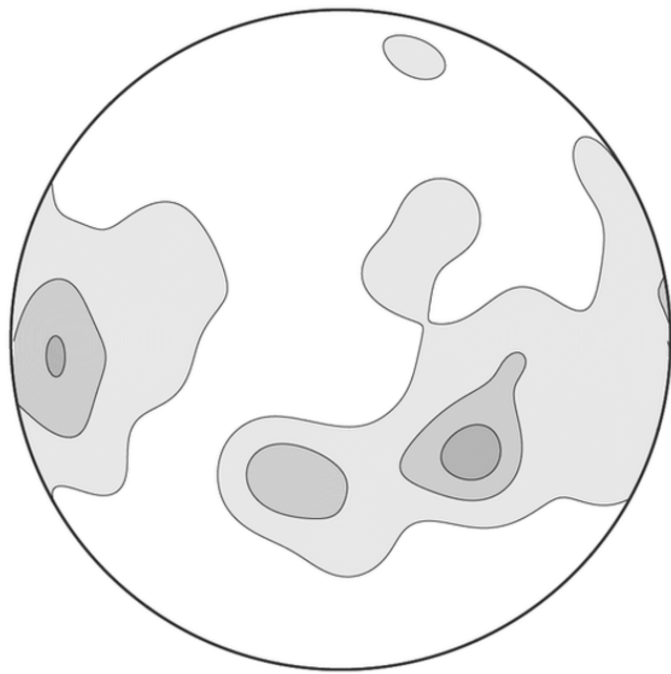


T3BC4A

Olivine



Clinopyroxene



T4BC4A

Clinopyroxene

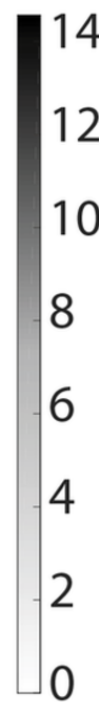
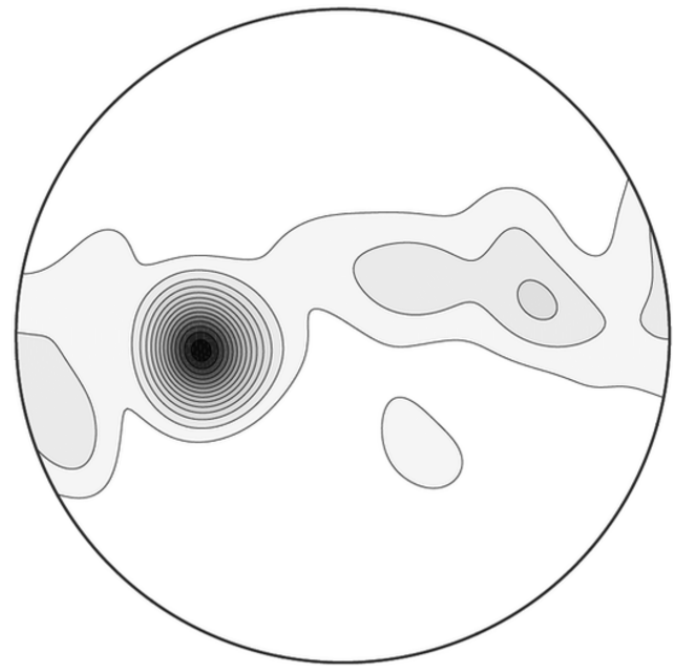
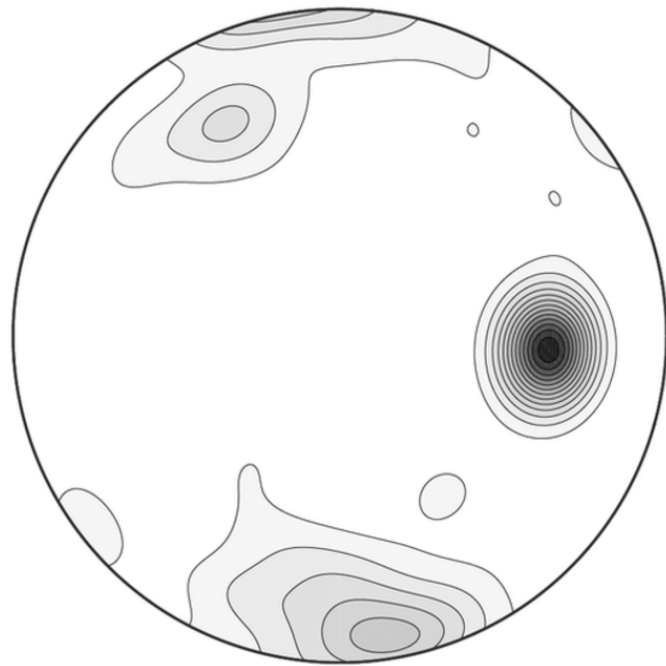
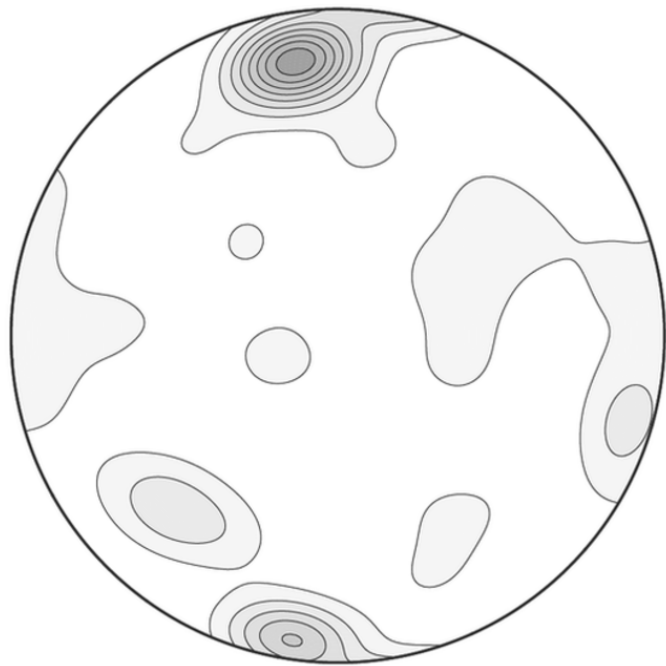


**Table 1: Lithology, texture and mineral abundance for the Bear Creek samples**

Sample	Lithology	Texture	Mineral abundance (%)*				
			Cpx	Opx	Olivine	Amphibole	Spinel
T4BC4A	Massive pyroxenite	Equigranular	95.66	0.74	2.98	0.61	0.01
T3BC4A	Massive pyroxenite	Equigranular	88.59	1.16	10.15	0.08	0.02
03T16A	Clinopyroxenitic intrusion	Pegmatitic	86.33	6.03	5.61	1.95	0.08
T4BC7B	Finely layered cumulates	Equigranular	89.2	0.56	6.1	4.12	0.02
03T46B	Finely layered cumulates	Equigranular	17.44	49.67	31.62	0.77	0.5
02T117A-coarse	Clinopyroxenitic intrusion	Pegmatitic	99.67	0.25	0	0.07	0.01
02T117A-cumulates	Finely layered cumulates	Equigranular	35.4	37.63	26.57	0.35	0.05
T3BC3A	Finely layered cumulates	Equigranular	58.44	26.61	12.56	2.37	0.02
01T13C	Finely layered cumulates	Equigranular	25.18	30.89	39.31	3.58	1.04
01T13B	Finely layered cumulates	Equigranular	81.13	6.01	8.87	3.88	0.11
01T13A	Finely layered cumulates	Equigranular	54.33	19.29	11.42	14.88	0.08
T3BC1A	Finely layered cumulates	Equigranular	39.66	21.52	34.92	3.83	0.07
T4BC8A	Finely layered cumulates	Equigranular	23.16	56.2	20.03	0.58	0.03
01T12A	Finely layered cumulates	Equigranular	26.14	44.3	25.58	3.53	0.45
T4BC2A	Lherzolite	Porphyroclastic	25.44	25.83	44.92	2.27	1.54
T4BC3A	Lherzolite	Porphyroclastic	5.59	30.69	63.56	0.02	0.14

\* calculated on indexed EBSD data